Effect of oxygen dissolution on the mechanical behavior of thin Ti-6Al-4V specimens oxidized at high temperature: Experimental and modelling approach

Damien Texier, Abhishek Palchoudhary, J. Genée, Quentin Sirvin, Yinyin Zhang, Guillaume Kermouche, Daniel Monceau, Dominique Poquillon, Eric Andrieu

Effect of oxygen dissolution on the mechanical behavior of thin Ti-6Al-4V specimens oxidized at high temperature: Experimental and modeling approach

Damien Texier[a], Abhishek Palchoudhary[a], Julien Genée[a], Quentin Sirvin[a], Yinyin Zhang[b], Guillaume Kermouche[b], Daniel Monceau[c], Dominique Poquillon[c], Eric Andrieu[c]

[a] *Institut Clement Ader (ICA) - UMR CNRS 5312, Université de Toulouse, CNRS, INSA, UPS, Mines Albi, ISAE-SUPAERO, Campus Jarlard, 81013 Albi Cedex 09, France*
[b] *École nationale supérieure des mines de Saint-Étienne, LGF, CNRS UMR 5307, 42023 Saint-Étienne cedex 2, France*
[c] *CIRIMAT-UMR CNRS 5085, Université de Toulouse, ENSIACET, 4 Allée Emile Monso, BP 44362, 31030, Toulouse Cedex 4, France*

Abstract

Micromechanical characterization of the oxygen-rich layer (ORL) of a Ti-6Al-4V alloy due to high-temperature oxidation was investigated at room temperature. The tensile strength of the pre-oxidized specimens linearly decreased as a function of the surface fraction of ORL in relation to the gage section, demonstrating a competition between oxygen strengthening and embrittlement. Electron-probe micro-analyses and nanoindentation testing aimed at locally assessing the elastic and hardness response of the material as a function of the oxygen content. These properties were used in finite element simulations to quantify stress profiles within the oxygen-graded material for different ORL thickness/specimen thickness couples.

Keywords: Titanium alloy, Micromechanical testing, Oxygen dissolution, Oxygen embrittlement, mechanical modeling

1. Introduction

Titanium alloys are increasingly used in the manufacture of intermediate/high temperature structural components for the transportation industry due to their interesting mechanical strength for a density nearly two times lower than steels or nickel-based superalloys. In service, structural components made of titanium alloys can be exposed to elevated temperatures (300-600 °C) and oxidative/nitriding atmospheres, typically air or combustion gases [1, 2]. However, Ti and Ti alloys dissolve large amounts of oxygen and nitrogen (up to 15 % in weight for O (resp. 33 % in atomic) and 7.6 % in weight for N (resp. 16 % in atomic) in the α-phase) [3]. High solubility of these interstitial elements leads to their ingress in the metal, by diffusion from the metal/oxide interface to the component core at high temperature. An oxygen-rich layer (ORL) subsequently extends for depths typically one order of magnitude thicker than the oxide layer [4, 5, 6]. The ORL is particularly brittle for oxygen concentration greater than 0.5-0.6 % [7, 8] atomic and can significantly impair the mechanical strength and ductility of oxidized components [9, 10, 11, 12, 13, 14, 15, 16, 17, 18, 19, 20, 21, 22, 23, 24, 7, 25, 26]. Similar environmental effects are reported for nitrogen insertion [9]. This oxygen/nitrogen embrittlement and early cracking of the ORL subjected to thermomechanical stresses strongly drop-off the fatigue endurance and lifetime of pre-oxidized titanium or components during service in oxidizing atmospheres [10, 17, 20, 22, 21, 26]. The fatigue limit is related to the extension of the brittle region, *i.e.*, the region with an oxygen content greater 0.5-0.6 % atomic [7, 8]. Therefore, significant researches have been conducted on the prediction of the oxygen diffusion within titanium and thus the extension of the ORL for isothermal [27, 28, 29, 6] but also complex thermal paths [29]. However, intermediate/high temperature components undergo mechanical loads in different and complex ways that can also alter the oxygen profile and extension

*Corresponding author
Email address: damien.texier@mines-albi.fr (Damien Texier)

of the ORL due to (i) the formation of a nitrogen-rich region in the vicinity of the oxide/ORL interface subsequently decreasing the oxygen concentration at the metal/oxide interface [5, 30, 31, 32], and (ii) the change in apparent diffusion coefficient of O within Ti leading to deeper ORL under creep loading [31]. Application of a steady-stress during oxidation was recently found to promote the formation of a nitrogen-rich layer, thus limiting the oxygen content at the oxide/ORL interface (decrease from 25 to 10 at. % of O at the oxide/ORL interface for a load of 70 MPa at 650 °C [31]). The ORL extension and oxygen profile under thermomechanical loading are a central question and different techniques aimed at characterizing it : (1) the electron microprobe (EPMA) [33, 5, 7], (2) the energy dispersive X-Ray spectroscopy (EDS) [34, 35, 30], (3) the secondary-ion mass spectroscopy (SIMS) [36], and (4) the atomic probe (APT) [30, 32]. The knowledge and prediction of the ORL extension is required in a first approach to estimate the ORL cracking and the associated notch effect on the mechanical performance and fatigue life of oxidized titanium, considering the ORL as a non-load bearing section. However, a better mechanistic understanding of the early damage development within the ORL under thermomechanical loading is needed to better predict the service life of these materials. Evaluation of the evolution of the mechanical and physical properties of titanium with variation in oxygen over a broad spectrum of oxygen concentration is required for modeling and simulating the mechanical behavior of the oxygen-graded material, *i.e.*, the property-graded material. Oxygen insertion within titanium is known for decades to modify dilatation, resistivity and mechanical properties of titanium, in its commercially pure or alloyed version [9, 13]. Oxygen makes titanium harder even for tens of percent change in O concentration [9, 11, 13, 14, 15, 37, 38, 20, 21, 22, 6, 39, 40, 41]. This change in hardness properties has been investigated on bulk samples with constant but quite low oxygen content (0.7 % atomic maximum and even nearly 1.5 % atomic [40]) or on cross-sectioned pre-oxidized samples with a large range of oxygen concentrations from bulk concentration to 25-30% atomic [11, 14, 15, 20, 6, 41]. Oxidation then diffusion techniques on thin foils also aimed at probing the mechanical properties of oxygen-rich titanium up to 20 % at. with a homogeneous concentration in the bulk [15, 42]. Different models were proposed, either linear [27, 14, 22], parabolic [9, 6] or following a power law form [11, 15, 39] to link hardness properties to the oxygen content. Hardness was also found to be highly sensitive to the crystallographic orientation [39, 41]. A quantitative relationship was proposed by Magazzeni et al. [39] between hardness, crystal orientation represented as the declination angle, and local oxygen content using multi-modal map correlation. This change in hardness properties is highly important to document the strengthening of titanium due to oxygen insertion. However, the complex stress/strain field associated with indentation loading and the tension-compression anisotropy of titanium makes this local technique not sufficient to fully understand their oxygen embrittlement under tension loading [23]. As far as the elastic properties are concerned, oxygen was also found to increase the elastic modulus of titanium for low concentration of oxygen or for oxygen-graded titanium due to pre-oxidation [13, 43, 18, 44, 38, 45, 40, 41]. The Young's modulus increases by 4 to 5 GPa for each atomic percent of oxygen for low oxygen alloying [43]. Baillieux et al. reported a linear increase of the Young's modulus with the fraction of ORL within the specimen gage section for pre-oxidized specimens, the ORL being stiffer than specimen core using Resonant Frequency and Damping Analysis (RFDA) [45]. Instrumented nanoindentation in a continuous stiffness mode also aimed at confirming the increase in Young's modulus with oxygen content but also with change in crystal orientation [46, 47, 48, 49, 41]. This point is important for stress distribution within the graded-property material subjected to a mechanical load due to the core-shell effect associated with the presence of the ORL. Furthermore, oxygen was also found to change the critical resolved shear stress of basal, prismatic, and pyramidal slip systems [50, 23], subsequently improving the mechanical strength of the alloyed material [9, 10, 12, 13, 43, 16, 18, 38, 50, 23, 25]. Ren et al. [23] reported that change in 0.5 % atomic in oxygen lead to (i) an increase in pyramidal slip activity mainly attributed to the decreasing of $\mathrm{CRSS}_{pyramidal}/\mathrm{CRSS}_{prismatic}$ ratio and (ii) a limit in deformation twinning under compression testing. While low oxygen alloying was found to significantly improve the mechanical strength of high purity titanium, high oxygen concentration inherent to the ORL formation was reported to either improve or impair the mechanical strength of pre-oxidized specimen due to the concomitant action of oxygen strengthening and embrittlement [14, 24, 25]. The drop in mechanical strength due to pre-oxidation is generally reported for Ti alloys, *i.e.* Ti64 or Ti6242s, compared to high purity titanium. The deleterious effect of the ORL on the yield strength and ultimate tensile strength of pre-oxidized specimens was found, but not that significant, due to the marginal fraction of the ORL on a conventional size tensile specimen with square-millimeter size gage section. Therefore, working on thinner specimens increases the surface over volume ratio and weights more the contribution of the surface, *i.e.*, the ORL in the present case. This micromechanical approach will be used in the present study to try

Table 1: Nominal composition of the Ti-6Al-4V alloy (in %(wt)).

Element	Ti	Al	V	Fe	O	C	N
% (wt)	Balance	6.0	4.0	0.19	0.17	0.05	0.04

to better document the mechanical behavior of the ORL and its influence on the mechanical integrity of pre-oxidized specimens.

In the present study, the tensile behavior of the ORL was investigated using microtensile pre-oxidized specimens with different thicknesses and exposure durations at high temperature. Additional characterizations were conducted to correlate local chemical and mechanical information within the ORL such as the hardness and the reduced modulus. The identification of oxygen profiles aimed at simulating oxygen profiles for the different oxidation time/specimen thickness investigated pairs. In addition, the correlated local mechanical properties as a function of the oxygen concentration was used to simulate and evaluate the stress distribution for the different pre-oxidized specimens.

2. Experimental procedures

2.1. Material

The material used in the present study was an annealed Ti-6Al-4V rolled plate with a nominal composition reported in Table 1. The oxygen content was measured using a ONH836 Oxygen/Nitrogen/Hydrogen Elemental Analyzer from LECO using the inert gas (He) fusion technique. The material consisted in an acicular Widmanstätten α-β microstructure with millimeter-size colonies (ASTM of -3.5, *i.e.*, 1.2 mm), as depicted in Fig. 1.

Dogbone-shape microtensile specimens with a thickness of 1 mm were extracted from the rolled plate via electrodischarge machining (EDM). The longitudinal direction (LD) of the microtensile specimens was perpendicular to the rolling direction (RD) and their thickness parallel to RD. The geometry of the microtensile specimens is illustrated in Fig. 2(a). Specimen edges were ground down to a P1200 SiC grit paper to eliminate the EDM-affected region. Microtensile specimens were then thinned down to different thicknesses using a LOGITECH CL50© lapping machine equipped with a PP5GT precision Jig and SiC papers down to a P2400 grit paper. This preparation technique is fully detailed in ref. [51] and allows obtaining a repeatable surface finish and a highly controlled geometrical tolerance in terms of sample thickness. Four thicknesses have been studied, namely 100, 180, 280 and 480 µm.

Microtensile specimens were pre-oxidized at 750 °C for 5, 20, 100 and 200 h in order to generate different oxygen profiles within the Ti-6Al-4V samples. This temperature was relatively high for most in-service applications of Ti64 components. The microtensile specimens were cleaned in acetone and then in ethanol using an ultrasonic bath for 15 minutes each before oxidation. A Nabertherm C290 furnace with static atmosphere, *i.e.*, no air stirring but natural convection, was used for all the pre-oxidation treatments. All the specimens were pre-oxidized during the same batch, with interruptions for the different pre-oxidation durations. This point is particularly important for the reproducibility of the nitrogen segregation and/or precipitation at the metal/oxide interface, thus affecting both the oxidation kinetics and the oxygen concentration at the metal/oxide interface [5]. During the oxidation treatments, the microtensile specimens were hung at the two head radii with platinum wires and the temperature was measured with a K-type thermocouple. Oxide spallation occurred when air cooling after oxidation, regardless of the oxidation condition (No extra ventilator nor forced air). 85 to 90 % of the specimen gage was deprived of oxides after cooling, regardless of the oxidation condition. Few oxides flakes were still adherent at the surface for short oxidation times (less than 100 h). Owing to the low interfacial toughness of the TiO_2 oxide growing at 750 °C, remaining oxides, nearly debonded of the metal/oxide interface, were gently mechanically removed prior to tensile testing using plastic tweezers. In this way, microtensile specimens were all deprived of their external oxide layer and only the contribution of the oxygen dissolved within the pre-oxidized samples was investigated. It is worth mentioning that tensile specimens after spallation/oxide removal had a blueish aspect, testifying the presence of a thin oxide layer even after oxide spallation. Indeed, oxide spallation usually does not lead to total detachment of the oxide scale. Some remnants remain and can cause this blueish aspect. Specimen thickness was measured before oxidation and after oxidation plus oxide removal using a 1 µm-accuracy micrometer.

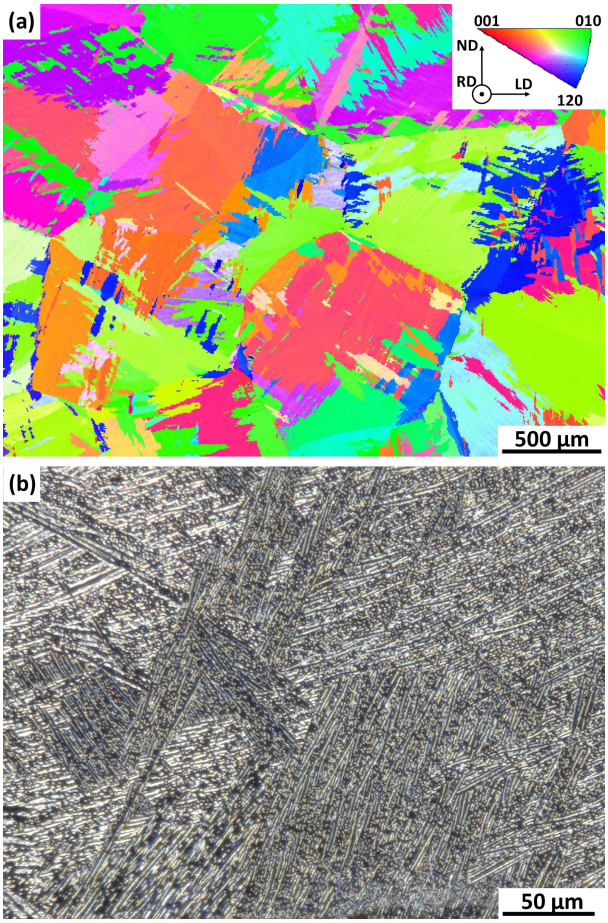

Figure 1: Microstructure of the Ti-6Al-4V material: (a) Grain microstructure represented as an inverse pole figures (IFP) map in reference to the loading direction (LD), (b) Optical micrograph showing the Widmanstätten microstructure on the same observation plane.

2.2. Microtensile testing paired with digital image correlation (DIC) techniques

Tensile experiments were performed at room temperature with a MTS Criterion model 43 electromechanical test system equipped with a 5 kN load-cell and self-tightening grips. Owing to the specimen thickness and brittleness, a gripping system using intermediate soft components between the specimen and the knurled grips was purposely adapted and depicted in Fig. 2(b), and fully detailed in Ref. [24]. For information, thinner and more exposed specimens were not possible to be tested due to failure prior to mechanical tests. For all the specimens, specimens were still complete prior to cooling. For the 100 µm-200 h specimens, they failed during the cooling phase. Spallation can be at the origin of the specimen cracking and the fracture surface of the samples were all brittle. For thicker and/or less exposed specimens, they failed during mounting on the tensile machine due to their high brittleness. They were still complete even after oxide removal and no particular crack was found at the specimen surface when observing using optical microscopy. The sensitivity to oxide spallation might depend on the specimen geometry.

Tensile tests were conducted under constant cross-head displacement rate of 3.5 µm.s^{-}1, corresponding to a strain rate of approx. 2×10^{-4} s^{-}1. Digital image correlation (DIC) techniques were used to obtain non-contact extensometry (macroscopic strain along the loading direction at the extremities of the gage length) and full-field strain measurements. Prior to tensile testing, white then black paints were applied onto the microtensile specimens using aerosol paints to form the random speckle pattern (see Fig. 2(c)). Numerical images with a resolution of 6000×4000 pixels^2 were acquired using a Nikon DS5200 camera and a Sigma 105 mm f2.8 DG MACRO lens using a 1 s intervalometer. Kinematic fields followed by strain fields were computed using PYXEL Python library developed by Passieux et al. [52]. The strain distribution within the gage section was visualized using ParaView, as shown in Fig. 2(d) for the non-oxidized specimen at 1.3 pct. total strain.

2.3. Microprobe analyses (EPMA)

EPMA samples were extracted from the elastically-deformed gage region of the microtensile, between the specimen head and the gage section. EPMA samples were mounted in an epoxy resin for cross-sectional preparation. The sample preparation was adapted using polishing down to P4000 grit papers, then 30 s of surface finishing with a 1 µm diamond paste to limit edge blunting and native TiO_2 formation. This finishing operation is important to better assess oxygen content in the vicinity of the metal/oxide interface [5]. The samples were coated with thin carbon layer then stored in a vacuum chamber (10^{-5} *mbar*) before EPMA analyses. Despite this particular care, some oxygen contamination can occur at the sample surface due to instantaneous formation of a native TiO_2 film. Therefore, the oxygen content inherent to this surface contamination and to the initial amount of O present in the as-received state, *i.e.*, before pre-oxidation, was corrected. An average of 5 measurements was taken at the core of the sample or on non-oxidized Ti-6Al-4V sample, *i.e.*, where the oxygen content was unaffected by oxygen diffusion during the pre-oxidation. The spectrum intensity corresponding to the oxygen was then deducted from the spectrum for each EPMA measurement. The oxygen content presented in the paper do not correspond to the absolute oxygen content, but to the oxygen uptake due to oxygen dissolution during oxidation. In other words, the (absolute) oxygen content in the ORL corresponds to the initial oxygen concentration of the as-received material C_0 plus the oxygen uptake Δ[O] due to oxygen ingress with oxidation. In addition, development of ORL cracking before mechanical testing was verified using microstructural analyses and confirmed using kinematics fields in the early stage of deformation. This point is important in order to conserve a plane diffusion front of oxygen in the volume.

EPMA measurements were obtained using a CAMECA© SXFive FE at an acceleration voltage of 10 kV and a probe current of 20 nA. The volume of analysis was 900 to 1000 *nm* in lateral and 650 to 700 *nm* in depth. The calibration of elements in Ti-6Al-4V samples was done with Al_2O_3 for aluminum, TiO for titanium, pure V for vanadium, and Fe_2O_3 for O. The absolute error on the oxygen content is close to 0.2 atomic percent. Three profiles across the whole sample thickness were performed per sample. Measurement spacing was of 1 µm near the surface (first 20 µm beneath the oxidized surface) and of 5 µm in the bulk.

2.4. Nanoindentation testing

Nanoindentation testing was performed using a MTS DCM nanoindenter equipped with a Berkovich diamond tip. As for EPMA analyses, cross-sectional samples were extracted from the elastically-deformed region of the microtensile samples. The samples were then cold mounted and ground using grit papers

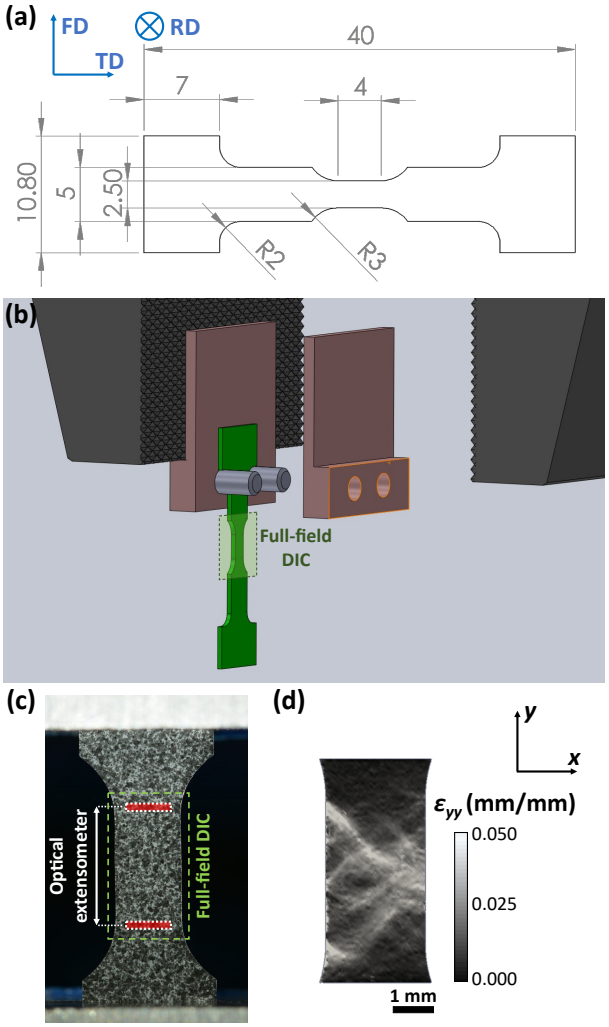

Figure 2: (a) Geometry of the tensile specimens, (b) illustration of the special gripping system for tensile testing of brittle specimens. The area used for full-field digital image correlation (DIC) techniques detailed in (c) is highlighted in green, (c) photographs showing the speckle pattern for full-field DIC techniques and the optical extensometer technique for macroscopic strain measurements, (d) example of strain distribution in the specimen gage of the non-oxidized specimen in the plastic domain along the principal loading direction.

from P120 gradually to P4000, followed by polishing using colloidal silica with 7.5% H_2O_2 + 5% HNO_4 for 10 minutes. The samples were then polished with water for 10 minutes to wash the sample surface. This surface finish is compatible both for EBSD characterizations and nanoindentation testing, limiting work-hardening in a shallow region beneath the polished surface. The measurement grid consisted in three filiations across the sample thickness with an indent spacing of 8 µm and a maximum indent depth of 300 nm (displacement control). This control mode, in comparison with force-control mode, is more adapted to have similar penetration depths for materials having high differences in local hardness and stiffness behavior. Base length of indentation imprints subsequently ranged between 1.9 and 2.0 µm, in the ORL as well as in the bulk material non-affected by oxidation. Elastic moduli and hardness were calculated from the load/displacement response during unloading of each indentation measurement following Oliver and Pharr formulations [53].

2.5. Scanning electron microscopy

Fractographic analyses were performed using a TM3030Plus tabletop scanning electron microscope from HITACHI© and a field emission gun-scanning electron microscope (FEG-SEM) NanoNOVA SEM from THERMO FISHER SCIENTIFIC© in a secondary electron (SE) mode at 15 kV.

Electron backscattered diffraction (EBSD) analyses were conducted using a FEG-SEM ZEISS© Supra 55-VP with an accelerating voltage of 20 kV and a step size of 3 µm. The sample preparation used for EBSD analyses was similar to the one for nanoindentation samples.

2.6. Finite element calculations

The motivations of the finite element calculations are twofold: (1) to evaluate the oxygen profile in thin Ti samples leading to an increase of the oxygen content in the bulk, *i.e.*, in conditions different from the semi-infinite medium hypothesis, and (2) to evaluate stress distribution profiles in the oxygen-graded material for different fractions of ORL, *i.e.*, different pre-oxidation/specimen thickness conditions. Indeed, oxidation of thin specimens can lead to an increase in oxygen content in the bulk, leading to deviation of analytical solutions to estimate oxygen profiles due to solid-state diffusion [54, 55]. Therefore, finite element (FE) solving methods were used to simulate diffusion profiles with CASTEM [56] for different oxidation durations and specimen thicknesses of specimens, with a special attention to thin specimens/large exposure time leading to increase of the oxygen concentration in the bulk material. Two dimensional simulations were conducted, the specimens being meshed using 4 node square isoparametric elements. The concentration at the metal/oxide interface and the diffusion coefficient of O within Ti were identified using EPMA analyses on thick pre-oxidized samples, *i.e.*, sample in semi-infinite diffusion conditions for the investigated temperature and durations (see section 3.4). For the FE calculations of the oxygen profile along the sample thickness direction, a constant oxygen concentration of 25 % at. was imposed as a boundary condition on the node line corresponding to the metal/oxide interface. In addition, a condition of symmetry was imposed at the center of the specimen (zero oxygen flux). The corresponding diffusion coefficient used was 3.89×10^{-15} USI.

These oxygen profiles were then used in a second set of FE calculations to compute the elastic tensile behavior of the oxygen-graded specimens, with stiffness evolving proportionally to the local oxygen concentration. A user-defined isotropic elasticity behavior was used: elastic properties were implemented as a function of the oxygen content, identified analytically using nanoindentation characterizations. Specimens were meshed using eight-node plane strain elements. The loading direction was applied normal to the oxygen flux and a condition of symmetry was imposed at the center of the specimen. Boundary conditions were also applied to avoid rigid body motion of the specimen and an arbitrary tension load σ_0 was applied at its end. Thus, normalized stress profiles are extracted under tensile loading, for the different conditions.

3. Experimental results

3.1. Tensile behavior of pre-oxidized specimens

Tensile tests were conducted at room temperature on specimens with thicknesses of 480 µm, 280 µm, 180 µm, and 100 µm and with different pre-oxidation durations. This approach aimed to document the tensile response of pre-oxidized specimens with different fractions of ORL. The stress-strain curves for all the pre-oxidized specimens are shown in Fig. 3 and compared to the tensile behavior of the non-oxidized specimens. Non-oxidized specimens were considered as the reference specimens to evaluate the influence

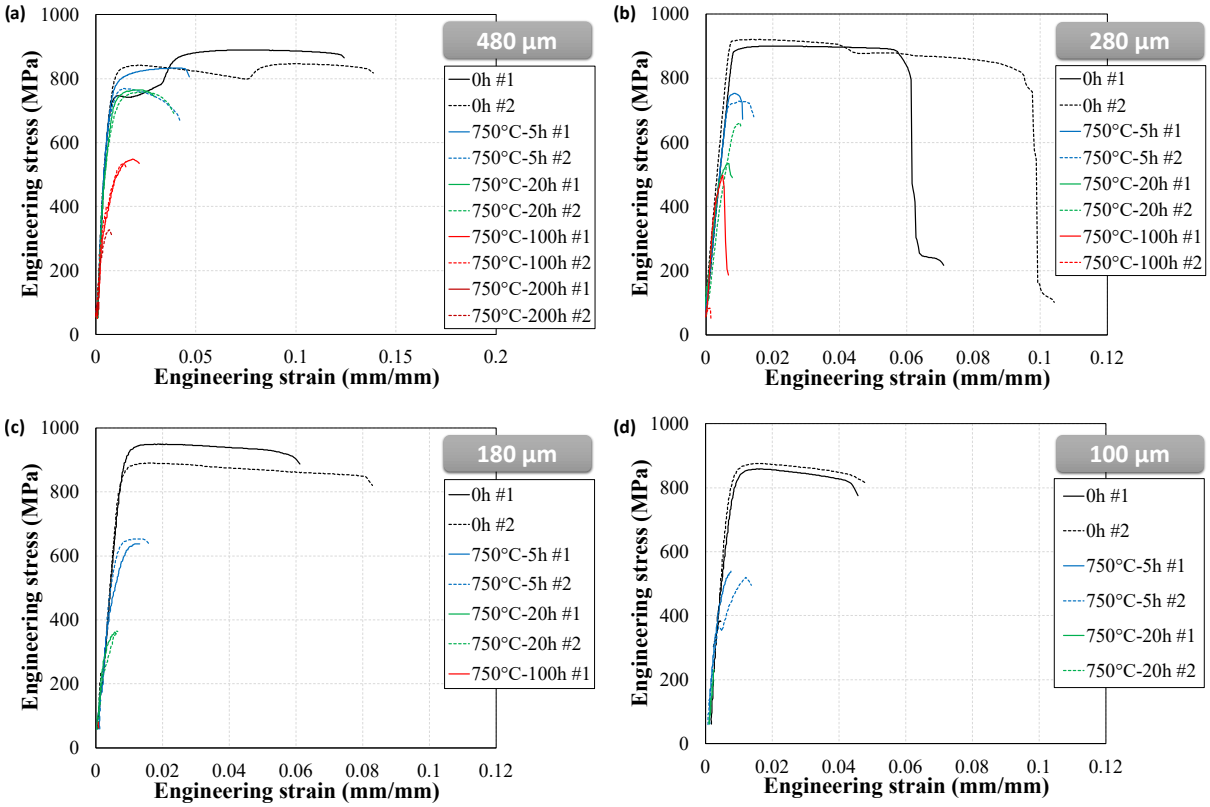

Figure 3: (a) Stress-strain curves of non-oxidized and pre-oxidized Ti-6Al-4V specimens with an initial thickness of (a) 480 µm, (b) 280 µm, (c) 180 µm, and (a) 100 µm showing both oxygen embrittlement and loss in mechanical strength due to high temperature exposure.

of the oxygen ingress into titanium on the mechanical response of the oxidation-affected specimens. This choice of reference state does not include potential metallurgical aging due to exposure at 750 °C. Discrepancy in stress-strain curves was observed at yielding and in the plastic domain for the non-oxidized specimens. Such differences were attributed to the non-statistically representative specimen with regard to the microstructure dimensions (millimeter-size grains while $4 \times 2.5 \times 0.3$ mm^3 sampled volume). However, the strain-to-failure (STF) is large enough and the tensile strengths (yield strength (YS) and ultimate tensile strength (UTS)) are close enough to be compared with the ones of the pre-oxidized specimens regardless of the specimen thickness. Interestingly, size effects on the non-oxidized specimens were found very little based on the size of the Widmanstätten colonies.

For pre-oxidized specimens, a significant drop in mechanical strength and ductility was found when either increasing the oxidation time or decreasing the specimen thickness. It is worth reminding that the oxide layer of the pre-oxidized specimens was removed prior to tensile testing and the gage section took into account the metal recession due to oxidation. Therefore, the obtained tensile responses of the pre-oxidized specimens typically demonstrated the influence of the ORL on the mechanical performance of Ti-alloys without the contribution of the oxide layer.

Macroscopic tensile properties, *i.e.*, the yield strength (YS), the ultimate tensile strength (UTS), and the strain-to-failure (STF), were measured from the stress-strain curve and were reported in Fig.4. As aforementioned, high temperature exposures in air were found to significantly decrease all the macroscopic tensile performances (YS, UTS, and STF) and this mechanical loss increased with the exposure duration. Therefore, the drop in tensile strengths is more pronounced for thin and oxidized specimens. An exposure of 5 hours at 750°C led to a drop in YS of approx. 8.5 %, 22 %, 34 %, and 37 % for 480 µm-, 280 µm-, 180 µm-, and 100 µm-thick specimens, respectively. For 20 hours exposure, the drop in YS is of 11 % and 80 % for the thickest and thinnest specimens, respectively. For exposures of 100 h and 200 h, thin specimens were not possible to be tested due to their considerable brittleness (specimen failure during handling/mounting). Similar trends were found for the UTS as a function of the specimen

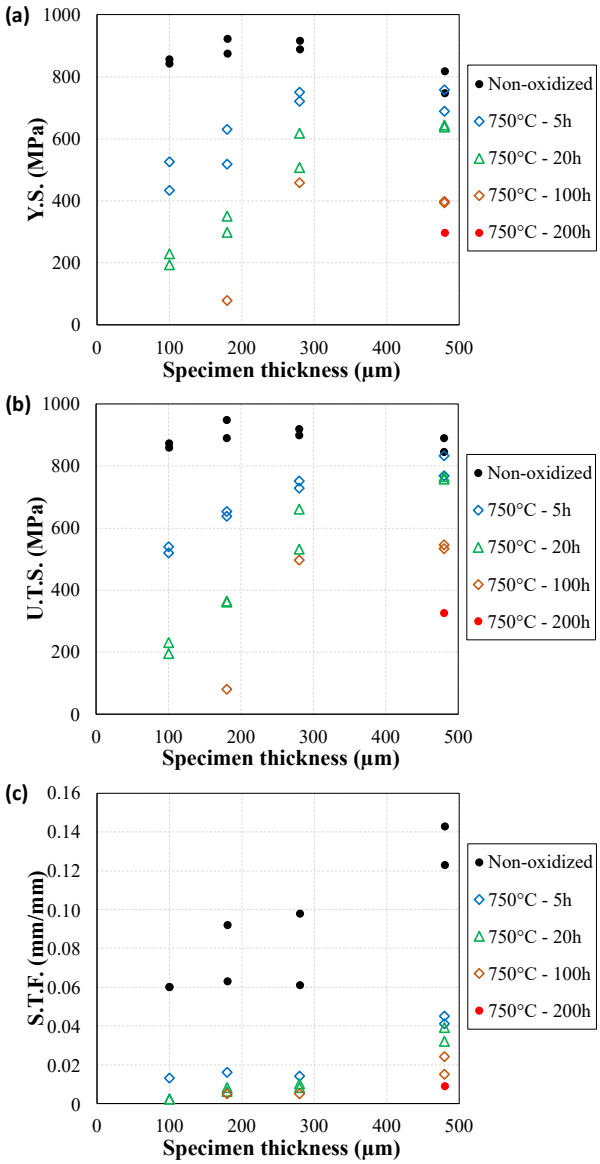

Figure 4: Evolution of the macroscopic tensile properties, *i.e.*, (a) the 0.2 pct. offset yield strength (Y.S.), (b) the ultimate tensile strength (U.T.S.), and (c) the strain-to-failure (S.T.F.) for all the specimen thicknesses and pre-oxidation durations showing both the thickness and pre-oxidation debit in mechanical performances.

thickness and the pre-oxidation duration.

3.2. Strain distribution of pre-oxidized specimens during tensile loading using DIC

Oxygen ingress within titanium was found to significantly impair the mechanical performance of the pre-oxidized specimens under tension. Therefore, local information on the deformation and damaging processes at different deformation levels is of interest. Digital image correlation was thus performed during the monotonic loading to measure the macroscopic strain as an optical extensometer on the whole gage length, but also to gain information on the local strain distribution (full-field measurement) for the different pre-oxidation conditions. The local mechanical response of pre-oxidized specimens was depicted for non-oxidized (black representation), 5 h (blue representation) and 100 h (red representation) pre-oxidation conditions at 750 °C for the 280 µm-thick specimens (Fig. 5(b) to (e)) for different stress/strain levels depicted in Fig. 5(a). The macroscopic stress-strain curves of the non-oxidized and 5 h pre-oxidized specimens are relatively smooth. The one of the 100 h pre-oxidized specimen exhibits stress-strain jumps when deforming, but also a higher apparent elastic modulus in the early deformation stage. Full-field

measurements aimed at evidencing differences in strain distribution on the specimen gage for the three pre-oxidation conditions. No strain concentration was found in the early stage of deformation (point #1) for all the pre-oxidation conditions, confirming that no-crack due to the pre-oxidation treatment is observed. Interestingly, the non-oxidized specimen exhibits inclined bands presenting intense strain localization. These bands, initiating below the macroscopic yield strength of the material, intensify with the deformation and correspond to the slip activity confined within prior β-grains/colonies. Such strain localizations are representative of slip-band dominated deformation mechanisms and confined in individual grains due to the acicular Widmanstätten microstructure. The diffuse character of the strain localization within an individual grain is due to the accumulation of active slip bands close to each other but also technical means (speckle, spatial resolution, numerical resolution). Despite strain localization due to slip activity, the deformation is much more homogeneous compared to pre-oxidized specimens, leading to higher macroscopic ductility. For the 100 h pre-oxidized specimen, horizontal strain localization depicts transverse cracking of the ORL (mode I) and are correlated to stress drop on the macroscopic stress-strain curve. When further loading, this crack continues to open and other cracks develop as well. Such intense strain localization due to early ORL cracking explains the non-homogeneous deformation of such pre-oxidized specimens and thus their low ductility. After 5 h pre-oxidation, horizontal cracks also occur at higher stress level, but not fully transverse (black arrows on ϵ_{yy} field blue#2). The horizontal strain localization appears confined within prior β-grains/colonies and inclined strain bands appears at higher macroscopic strain levels, similarly to the one of non-oxidized specimens.

3.3. Fractographic analyses of the pre-oxidized specimens

Based on the strong change in strain-to-failure for pre-oxidized specimens, fracture surfaces were observed for all the specimens, *i.e.*, both non-oxidized and pre-oxidized specimens. The fracture surface of the non-oxidized specimens presents typical dimples and interlamellar fracture features on the whole fracture surface (Fig. 6(a & d)). Severe and local necking was observed on the fracture surface of non-oxidized specimens, thus reminding the coarse grain microstructure of the present Ti64 alloy. For comparison, pre-oxidized specimens depict relatively rectangular fracture surface with less pronounced necking. Fracture surfaces of pre-oxidized specimens are divided in a ductile region in the core of the specimens and a peripheral brittle region corresponding to the ORL cracking (Fig. 6(b & e)). Longer exposure at high temperature lead to deeper ORL, and subsequently greater extension of the brittle layer. 480 µm-thick specimens keep a ductile character in the specimen core regardless of the pre-oxidation for the present experimental conditions. An insignificant core region remains ductile after 100 h oxidation for the 280 µm-thick specimens while the fracture surface of the 200 h pre-oxidized specimen is fully brittle. When comparing all the specimens with the different thicknesses and pre-oxidation durations, fully brittle fracture surfaces are noticed for the following ratio "200 h/280 µm", "100 h/180 µm" and "20 h/100 µm". In addition, the brittle layer is also divided into a (i) flat and smooth brittle surface in the extreme surface with fracture topography independent of the microstructure, and a (ii) rougher fractured region immediately below with fracture path following the lamellar structure of the material. In the present work, EPMA measurements were also conducted to characterize oxygen profiles (Fig. 9(a)). The direct comparison between fracture surface analyses and oxygen profile will be done in the discussion section.

Image analyses were performed on all the fracture surfaces in order to quantify the extent of both the flat brittle region in the extreme surface and the whole brittle region. The ORL extension, assumed here as the whole brittle region, $\xi_{Brittle}$, was considered here as the distance from the surface to the transition between the brittle and ductile region on the fracture surface, this latter showing dimples. Similarly, the extension of the flat brittle region was considered here as the distance from the surface to the transition between the flat brittle and rough brittle region on the fracture surface. The extension of the whole brittle region linearly increases with the square root of the exposure time t, as depicted in Fig. 7(a) and described in equation 1 [57].

$$\xi_{Brittle} = \sqrt{D_{app} t} \tag{1}$$

with $D_{app}(750\,^{\circ}\mathrm{C}) = 172.9\ \mu\mathrm{m}^2\mathrm{s}^{-1}$. The yield strength of the specimens for the different pre-oxidation conditions were plotted as a function of the square root of the time (Fig. 7(b)). Specimens with a thickness of 480 and 280 µm clearly highlight the influence of the pre-oxidation time, *i.e.*, the extension of the ORL on the drop in mechanical strength due to early oxygen embrittlement. Thinner specimens show a greater impact of the ORL on their mechanical integrity due to the higher fraction of ORL compared to

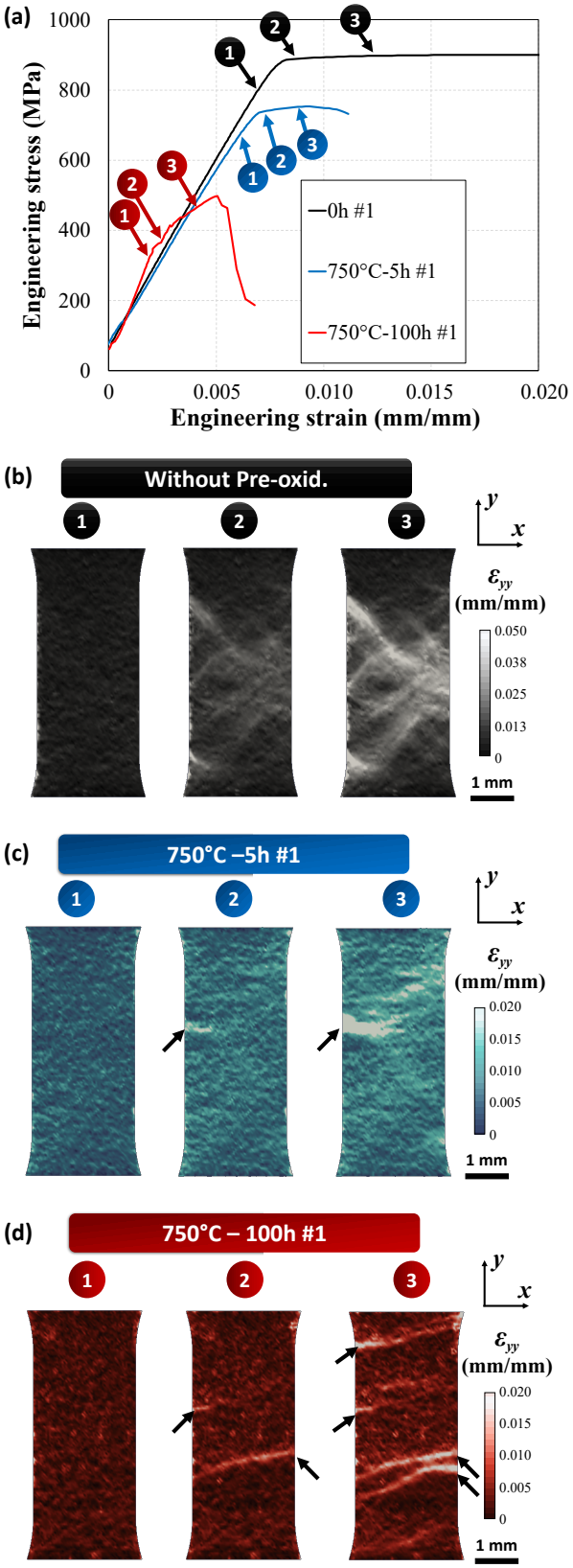

Figure 5: Local strain maps obtained using DIC measurements at different stress-strain levels for non-oxidized and oxidized Ti-6Al-4V specimens with an initial thickness of 280 μm.

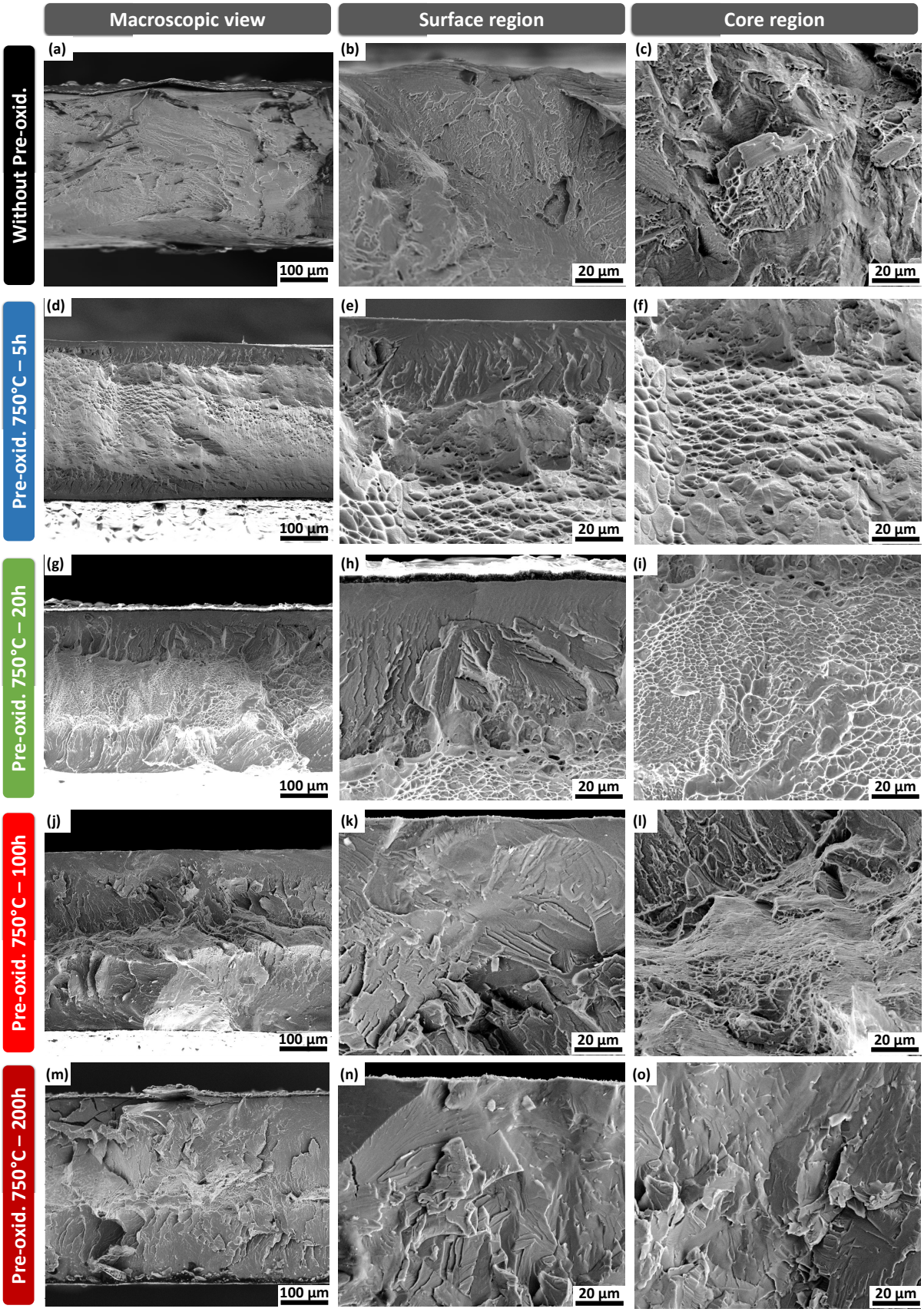

Figure 6: Fracture surface observation of non-oxidized and oxidized Ti-6Al-4V specimens showing the transition from brittle to ductile fracture features associated with the extension of the ORL.

the specimen thickness. Therefore, the yield strength of the different pre-oxidized specimens was plotted as a function of fraction of ORL in a specimen gage section (Fig. 7(c)). Interestingly, the yield strength is proportional to the fraction of ORL in a specimen gage section.

3.4. Gradient of oxygen content due to oxygen dissolution in the metallic material

The motivation of EPMA analyses to quantify oxygen profiles is to extract the coefficient of diffusion of O in Ti64 in thick specimens in order to be representative of the semi-infinite medium in order to analytically determine the coefficient of diffusion from the Fick's law [54, 55]. Therefore, oxygen profiles across the thickness of the 480 µm-thick specimens were characterized for all the pre-oxidation durations at 750 °C, *i.e.*, 0, 5, 20, 100, and 200 hours. Thinner specimen might not respect the semi-infinite medium condition, thus failing in the accurate identification of the coefficient of diffusion. Three EPMA profiles were performed per pre-oxidation condition, as depicted in Fig. 8(a). Oxygen profiles were then plotted as a function of the distance from the metal/oxide interface for identification of the coefficient of diffusion of O within Ti (Fig. 9(a)). Similar oxygen concentrations at the metal/oxide interface ($\approx$ 25 % at.) were found for all the pre-oxidation durations, testifying the reproducibility in pre-oxidation and nitrogen segregation/precipitation. Therefore, the focus was on the oxygen distribution in the ORL. A unidirectional solid-state diffusion scheme was considered. The oxygen flow was considered to be proportional to the gradient of O within Ti and is governed by Fick's law [54, 55]. A solution of this equation, in the case of the diffusion in a semi-infinite solid with a constant surface concentration C_s and a diffusion coefficient D independent of the concentration and the position x leads to Fick's law equation :

$$\frac{C_x - C_0}{C_s - C_0} = 1 - erf(\frac{x}{\sqrt{4Dt}}) \tag{2}$$

where C_x is the concentration of the species that diffuse at position x after a time t, C_0 is the concentration at the core of the sample in the semi-infinite medium. Similar C_s were found regardless of the pre-oxidation time ($C_s \approx 25$ % at.), but the extension of the ORL increased with the exposure time. The coefficient of diffusion of O within Ti was calculated from each profile individually, for each profile per pre-oxidation condition. The average coefficient of diffusion and scattering of O within Ti for the different pre-oxidation conditions was found of $D = 1.10 \pm 0.3{\cdot}10^{-15}$ m^2.s^{-1}. This coefficient of diffusion is in good agreement with the one reported in the literature [57].

3.5. Nanoindentation testing of the ORL

Nanoindentation tests were performed for the different pre-oxidation conditions to document the local mechanical response of the material with different oxygen contents, *i.e.*, the elastic modulus (Fig. 8(b)) and the hardness (Fig. 8(c)). Some discrepancy in the elastic moduli and hardness was found even in the bulk, region non-affected by the oxygen ingress. This scatter can arise from differences in crystallographic orientation of the indented grains from a sample to another one. Both the properties increased with the oxygen content. Interestingly, the hardness was found to be more affected than the elastic properties due to the oxygen increase. Indeed, the hardness near the metal/oxide interface is 2.8 times greater than in the bulk while the elastic modulus is 40 % greater. Knowing the position of each indent as a function of the metal/oxide interface, it is thus possible to express both the elastic properties and hardness as a function of the oxygen content (Fig. 9(b) and (c), respectively). The elastic modulus was found to evolve as a function of the oxygen concentration, from 130 GPa in the bulk to 187 GPa for 25 % at. addition of oxygen. The elastic modulus $E([O])$ (in GPa) can thus be express as follows :

$$E([O]) = 130 + 2.3 * [O] \tag{3}$$

with $[O]$ the oxygen concentration in atomic pct.. This relationship will be further used in numerical simulations to document stress distribution for the different conditions. Similarly, the hardness $H([O])$ (in GPa) can be expressed as a function of the oxygen content and follow a parabolic expression as follows :

$$H([O]) = 5.5 + 0.34 * [O]^{1/2} \tag{4}$$

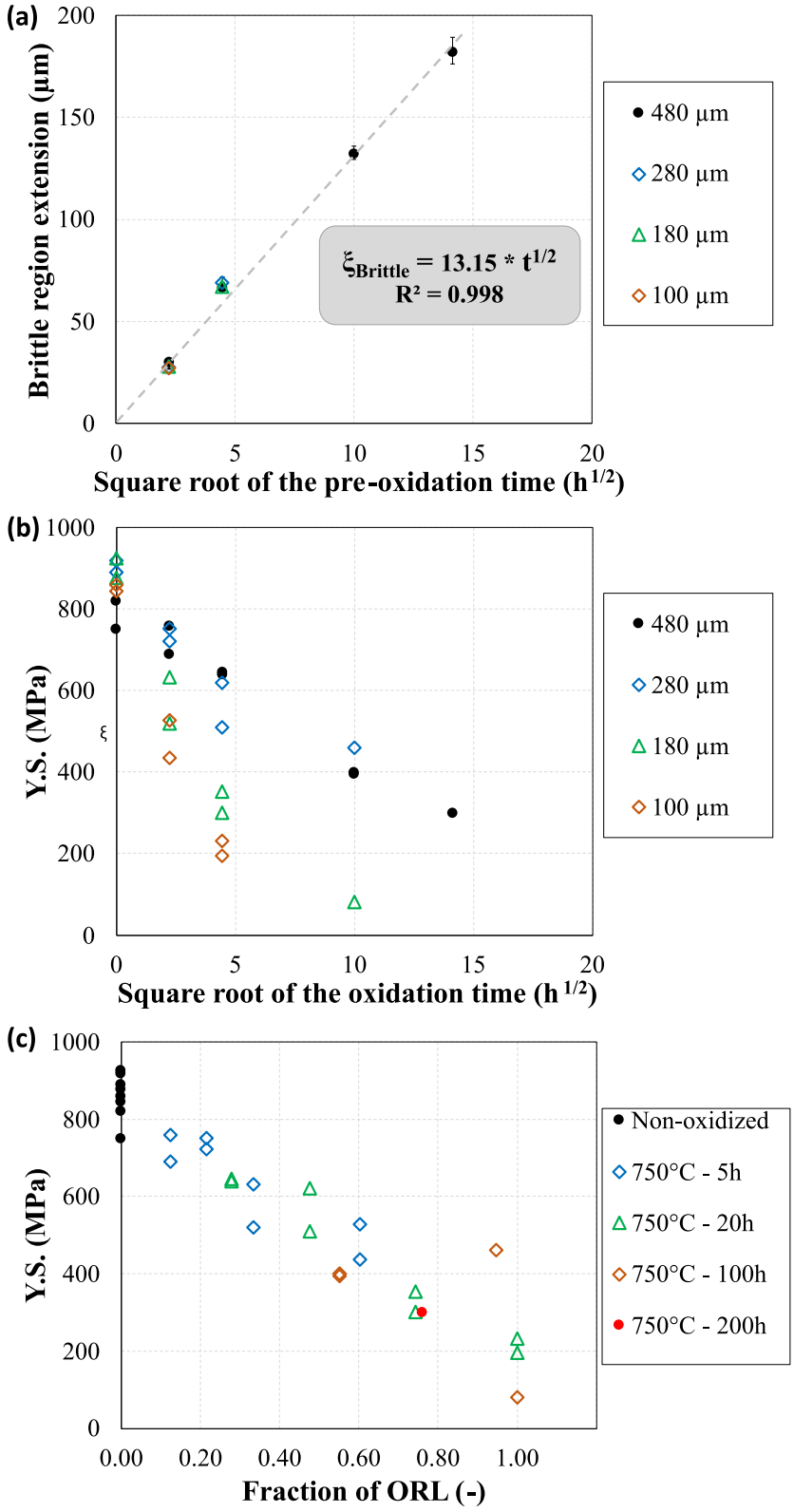

Figure 7: (a) Extension of the brittle region as a function of the square root of the pre-oxidation duration. (b) Evolution of the 0.2 pct. offset yield strength (Y.S.) as a function of the square root of the pre-oxidation duration for all the specimen variants.(c) Evolution of the 0.2 pct. offset yield strength (Y.S.) as a function of the fraction of ORL across the specimen thickness for all the specimen variants.

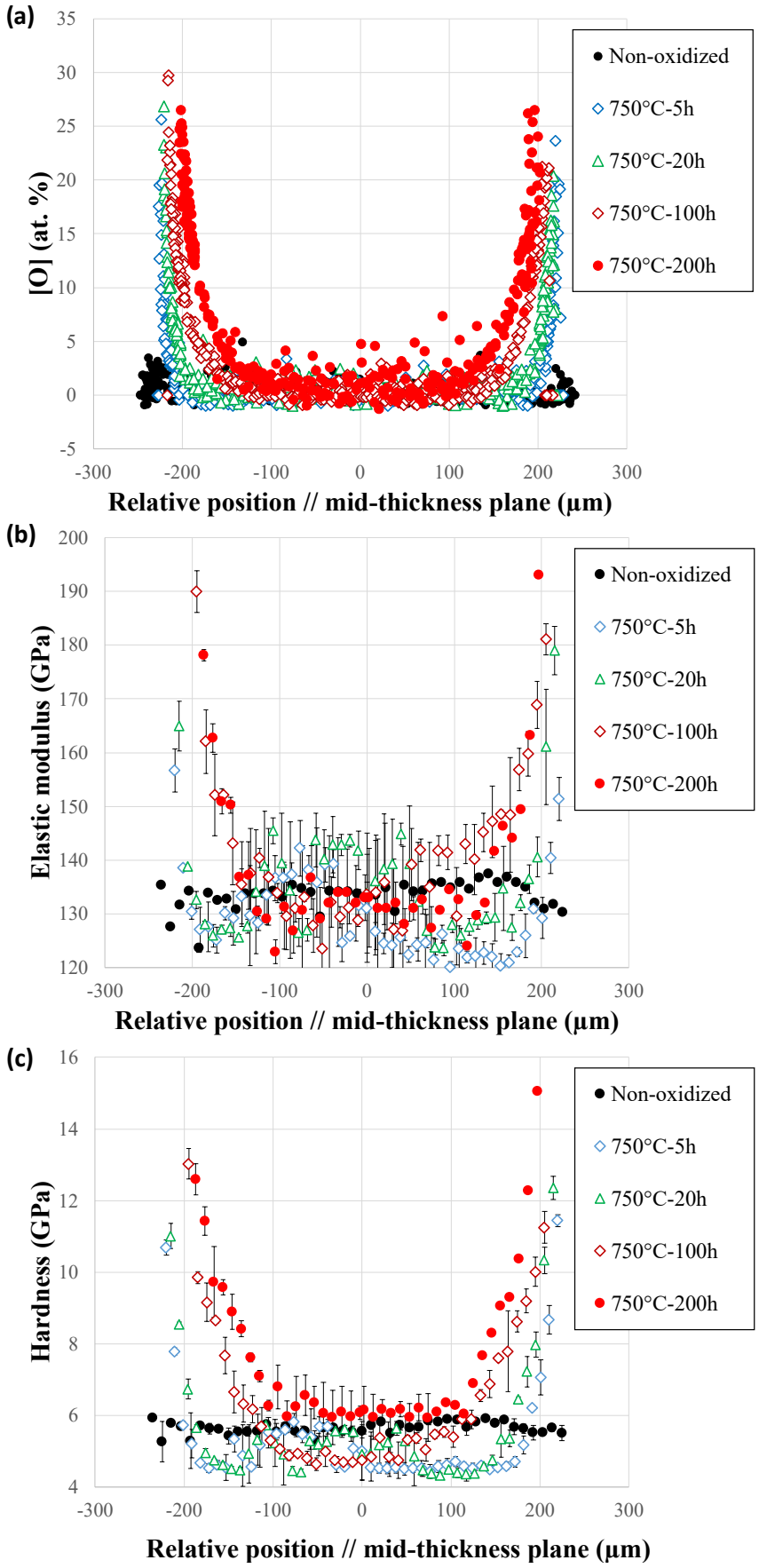

Figure 8: Through thickness chemical and local mechanical properties profiles for the different pre-oxidation conditions for Ti-6Al-4V specimens with an initial thickness of 480 µm : (a) Oxygen profiles obtained using EPMA, (b) Elastic modulus profiles, (c) Hardness profiles.

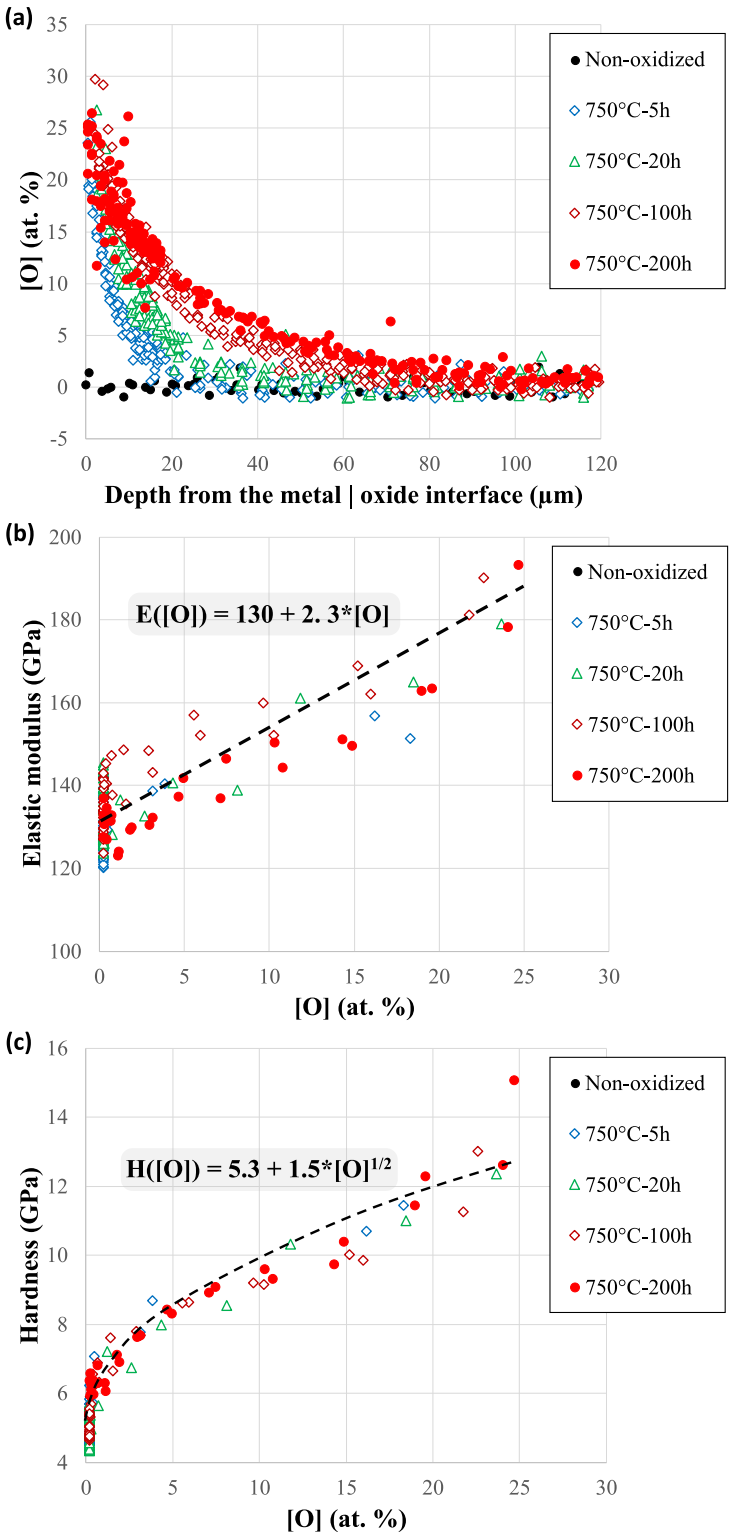

Figure 9: (a) Oxygen profiles of the pre-oxidized specimens as a function of the distance from the metal/oxide interface. (b) Elastic modulus and (c) Hardness as a function of the increase in oxygen.

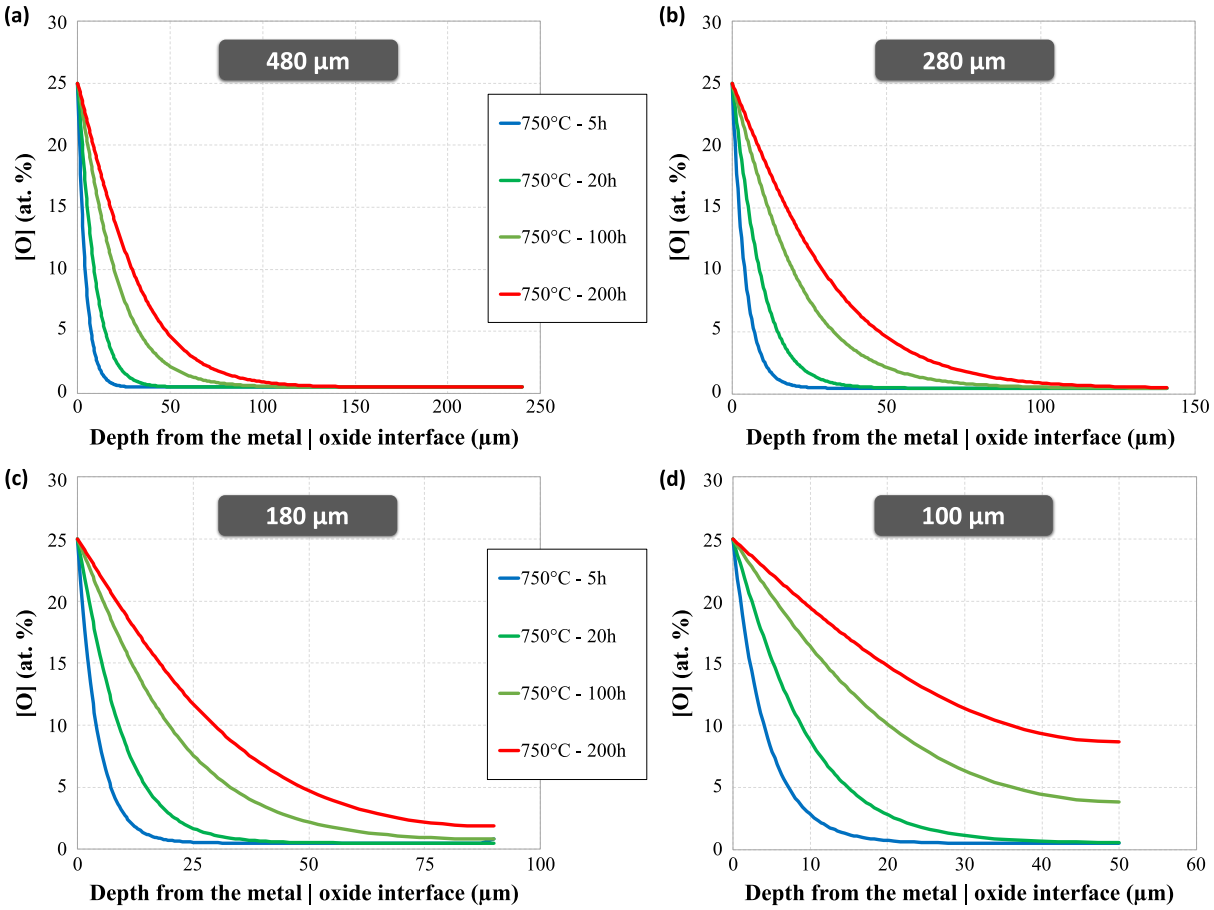

Figure 10: Oxygen profiles of the pre-oxidized specimens as a function of the distance from the metal/oxide interface. (a) 480-, (b) 280-, (c) 180-, and (d) 100-thick specimens.

3.6. Simulations of oxygen profiles and stress states under tensile loading

As aforementioned, numerical simulation of oxygen profiles is needed for thin specimens since the analytical solution (Fick's model) is not valid anymore when oxygen ingress affect the specimen core. The identification of the diffusion properties of O within Ti64 analytically identified on bulk specimens was used to evaluate the oxygen ingress within thin specimens for the different pre-oxidation conditions (Fig. 10). Specimens as thin as 180 µm experienced an increase in oxygen concentration of the specimen core for exposures longer than 100 h (Fig. 10(c)), conditions for which diffusion fronts meet in the specimen core (20 h for 100 µm-thick specimen (Fig. 10(d)), respectively). These numerical simulations validate the particular brittleness of thin specimens exposed for long periods.

The relationship between O content and elastic properties identified from nanoindentation testing was implemented in the numerical model to evaluate stress distribution within specimens with different "ORL extension/specimen thickness" ratios (Fig. 11). Stress decreases from the surface to the specimen core, typical of coated or graded materials experiencing a "core/shell" behavior. For a given thickness, stress at the surface was found maximal for shorter oxidation durations. Similarly, stress was also found maximal in the specimen core for shorter oxidation durations. The "core/shell" effect is enhanced when the ORL is thinner. In addition, size effects also affect the "core/shell" contribution. It consists in maximal stresses at both the specimen surface and specimen core for thicker specimens. 40 % increase in stress can be locally found in the vicinity of the surface for short oxidation time/thick specimens. Interestingly, stress was found maximal at the surface and specimen core for shorter exposure times and thicker specimens. In addition, oxygen increase in the specimen core for thin/long exposure specimens lead to higher stress in the specimen core, as illustrated in Fig. 11(d).

Another illustration of the numerical simulations was to compare size effects for a given oxidation exposure, as depicted in Fig. 12. For 20 h pre-oxidation, all the oxygen profiles overlapped together since the diffusion was not fast enough and the specimens thin enough so that diffusion fronts meet in

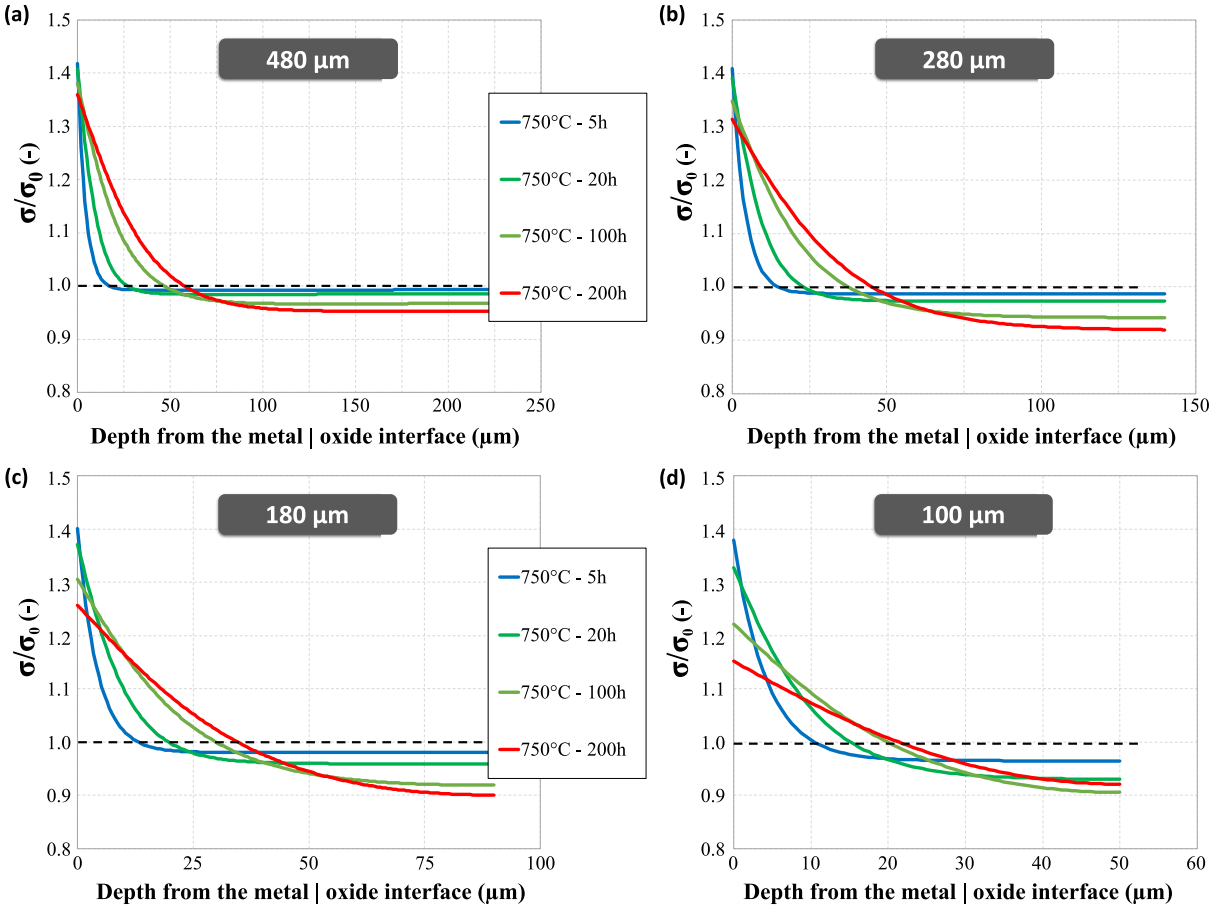

Figure 11: Stress profiles of the pre-oxidized specimens under tensile loading at a macroscopic stress σ_0 as a function of the distance from the metal/oxide interface. (a) 480-, (b) 280-, (c) 180-, and (d) 100-thick specimens.

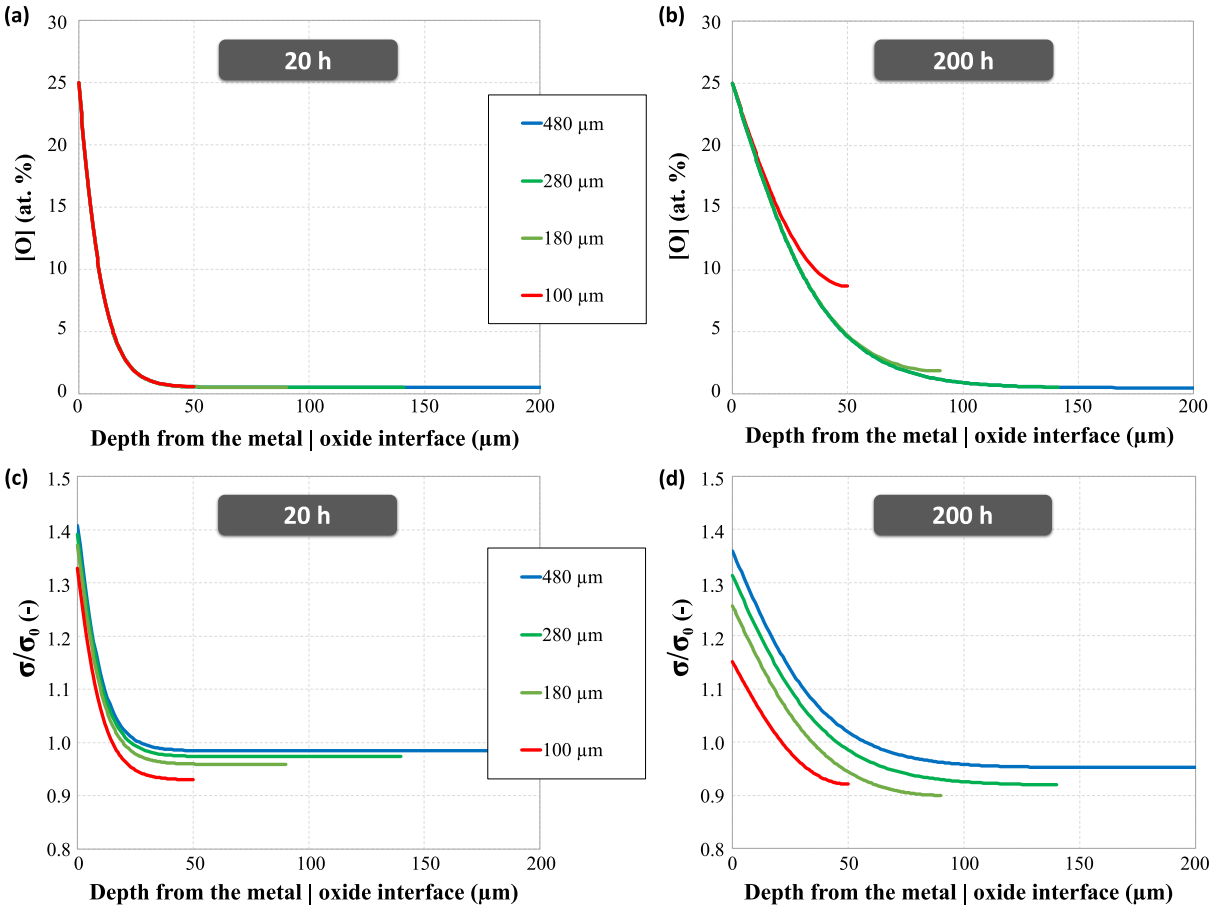

Figure 12: Oxygen content and stress profiles of the pre-oxidized specimens under tensile loading at a macroscopic stress σ_0 as a function of the distance from the metal/oxide interface for two oxidation exposures. (a) oxygen profile for 20 h, (b) oxygen profile for 200 h, (c) stress profile for 20 h, and (d) stress profile for 200 h.

the specimen core (Fig. 12(a)). This is not the case for longer exposure times, *i.e.*, 200 h, where oxygen enrichment was experienced for specimens as thin as 180 µm (Fig. 12(b)). Interestingly, stress is maximal at each depth from the metal/oxide interface for thicker specimens, as long as oxygen enrichment does not occur in the specimen core (Fig. 12(c)). Maximal stress at both the metal/oxide interface and specimen core are found for thicker specimens due to "core/shell" effects. For longer exposure times, oxygen enrichment in the specimen core can have an effect on the stress distribution and stress in the specimen core, as observed in Fig. 12(d). This interesting result does not consider the potential effect of the external TiO_2 scale, this latter being in compression due to growth onto the metal, affecting the overall stress state of the multi-layer/graded material.

4. Discussion

4.1. Oxygen insertion within titanium makes it stiffer

Micromechanical characterizations, *i.e.*, nanoindentation tests and microtensile tests, were performed in the present study in order to identify local mechanical properties within the ORL and to evaluate the effect of the ORL on the macroscopic response of pre-oxidized specimens. It is worth mentioning that nanoindentation tests evidenced an increase in material stiffness with the oxygen increase, as commonly reported in the literature for titanium with low oxygen contents but also for pre-oxidized titanium [13, 43, 18, 44, 38, 45, 40, 41]. In the present study, a linear assumption between the elastic modulus and the oxygen content (in at. %) was considered from experimental data (Fig. 9(b)). The elastic modulus was found to increase by 2.3 GPa for each atomic percent of oxygen from nanoindentation results. Lee et al. reported an increase of 4.7 GPa for each atomic percent of oxygen for relatively low alloyed Ti64, *i.e.*, between 0 and 3 at. % of oxygen [43]. Such greater influence of oxygen on the elastic response

was also found via nanoindentation testing for low oxygen contents per sample but was not considered here based on the lack of data and possibility of elastic anisotropy based on local colony orientation, as illustrated in Fig. 9(b). Elastic anisotropy at the sub-grain level has been clearly reported for nearly pure titanium (CP-Ti), Ti-alloys and pre-oxidized titanium alloys, and can contribute to a variation of ± 10 % in elastic modulus response depending on the collinearity of the c-axis with the nanoindentation direction [46, 47, 48, 49, 41]. Owing to the coarse microstructure in the present study, elastic anisotropy can partially explain the variability/offset of elastic response from sample to sample for similar oxygen contents.

4.2. Competition between mechanical strengthening and early damage

While both tensile and compressive mechanical techniques evidenced stiffer properties for O-rich Ti alloys, the mechanical strength of the pre-oxidized samples was found to be dependent on the loading application. Nanoindentation testing, *i.e.*, a multiaxial compressive loading, evidenced a strengthening within the ORL while the tensile strength of pre-oxidized specimens decreased with the specimen size reduction and/or the increase in oxidation time. Such a difference in mechanical response sheds light on the tension/compression anisotropy of the ORL due to change in atomic binding energy of Ti due to O insertion, leading to a change in metallic to ionocovalent binding. Therefore, the brittleness of the oxygen-rich Ti impairs the mechanical performance in tensile conditions more compared to compressive conditions. Interestingly, both the yield strength and ultimate tensile strength decrease with either the increase in oxidation time or the decrease in specimen thickness, testifying the so-called oxygen embrittlement due to ORL and subsequent reduction of the load-bearing section (Figs. 2, 3, 4, and 7). Such evolutions in mechanical strength with oxygen enrichment are not commonly reported in the literature :

- most of the studies focused on low oxygen content CP-Ti materials subject to solid solution strengthening, thus leading to an opposite effect on the tensile strength, *i.e.*, a strengthening with oxygen insertion [9, 10, 12, 13, 43, 16, 18, 38, 50, 23, 25] ;
- due to the significant thickness/diameter of conventional tensile specimens for pre-oxidized specimens, leading to very low fraction of ORL compared to the whole gage section and insignificant change in terms of mechanical strength but change in ductility due to oxygen embrittlement [7] ;
- due to the difficulty to elaborate structural Ti-based alloys with high oxygen contents and keeping a similar metallurgical state [43].

For CP-Ti and Ti alloys with high oxygen concentration, the mechanical strength of pre-oxidized specimens can either be improved or impaired due to the concomitant action of the oxygen strengthening and embrittlement [14, 24, 25]. The drop in mechanical strength due to pre-oxidation is generally reported for Ti alloys, *i.e.*, Ti64 or Ti6242s, compared to high purity titanium. Bendersky et al. have investigated the tensile performance of Ti64-alloy specimens pre-oxidized at 900 °C up to 20 hours. They demonstrated the formation of a continuous α-Ti layer beneath the metal/oxide interface, generally denoted as α-case. Despite similarity in mechanical performance evolutions with oxygen increase, the ORL layer differs in nature from an α-case layer since the present ORL conserved its β-metastable Ti. The direct confrontation in results is therefore not straightforward.

The present study has highlighted the drop in mechanical strength under tensile loading due to the thinness of the specimens, thus probing large fractions of ORL compared to the whole specimen gage section. The main difference between pre-oxidized CP-Ti and structural Ti alloys (Ti64, Ti6242S, etc.) is the work-hardening capability of the virgin material under tensile loading (Fig. 3), making structural Ti alloys particularly sensitive to notch effects and subsequently ORL cracking. Interestingly, the yield strength of the pre-oxidized specimens was found to linearly decrease with the fraction of ORL occupied on the specimen gage section, regardless of the oxidation time/specimen thickness conditions (Fig. 7(c)). This linear trend reveals the sensitivity of the pre-oxidized specimens to load-bearing surface based on the onset of ORL cracking in the elastic domain, thus leading to a reduction of the effective gage section with the oxidation time/specimen size reduction. To the best of the authors' knowledge, such trends were not reported in the literature and demonstrate the use of micro-sized/ultrathin specimens to document oxygen embrittlement. Combining oxygen profiles from EPMA analyses (Fig. 8(a)) and brittle regions identified on the fracture surfaces (Fig. 7(a)), it is possible to define a critical oxygen content for the extension of the different brittle regions, *i.e.*, the flat brittle region and the rough brittle

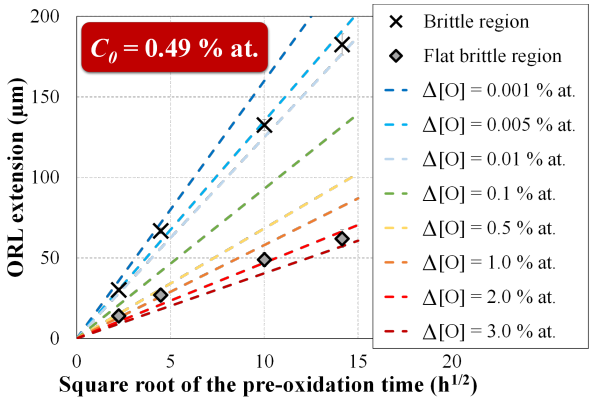

Figure 13: Extension of the brittle regions, *i.e.*, flat brittle region and overall brittle region, and of the ORL for different oxygen uptakes Δ[O] as a function of the pre-oxidation time. For information, the oxygen concentration in the bulk is of 0.49 % at.

one (Fig. 13). The oxygen uptake measured, Δ[O], at the brittle-ductile transition for the different pre-oxidation conditions is of 0.005 % at., leading to a critical oxygen concentration of (0.495 % at. of O, *i.e.*, the bulk concentration C_0 of 0.49 % at. plus the oxygen uptake Δ[O] of 0.005 % at.). This critical oxygen concentration is almost similar to the one reported by Casadebeight et al. ($[O]_{crit}$ ≈ 0.5-0.6 % at. [7, 8]). Indeed, the authors defined the critical concentration using EPMA analyses at $(C_x\text{-}C_0)/(C_s\text{-}C_0) \approx 0.005$, *i.e.*, $C_x \approx$ 0.5-0.6 % at. based on the usual oxygen concentration in the bulk and at the metal/oxide interface. The authors also provided an extensive investigation of the ORL extension using EPMA, fracture surface and secondary crack penetration on cross-sectional observations. They found less affected brittle regions from fracture surface analyses but slightly deeper oxygen diffusion compared to the present study. This difference in extension of the whole brittle region can arise from the microstructure. In the present study, the lamellar microstructure and the large former-β grains studied here can impede the evaluation of the brittle region once the brittle fracture is already initiated in the lamellar microstructure or the ease of crack propagation of the brittle crack in the lamellar structure within the same colony with a low-oxygen content. In addition, α-Ti has a greater oxygen solubility compared to β-Ti [3]. This particular two-phase microstructure can also influence oxygen ingress inside the material either by volume diffusion/solubility limit in each phase or by α/β interfacial diffusion. However, the present study did not allow to inform and clarify this point. Further investigations are required for a better understanding of the crack initiation then propagation within the ORL as a function of the oxygen profile and content. In addition, the critical oxygen concentration at the transition between the flat-rough brittle region is of 3.5 % at. and describe the transition from a fracture mode insensitive to sensitive to the lamellar structure. This flat brittle region is highly brittle and is of great importance to be characterized for structural components exposed at intermediate temperature.

An advantage of ultrathin but large specimens lay in the statistical representation of the microstructure in the whole gage section compared to micro-sized specimens, generally probing one or few grains/microstructural features. This point is important based on the coarseness of the Ti64 microstructure with grain/colony sizes comparable or even larger than the specimen thickness but not width and length. Such coarse microstructure lead to particular strain/slip localization at the grain-scale, leading to a high variability of microplasticity onset, as depicted in Fig. 5(b) for the virgin Ti64. This point will be further discussed in the following sections. Micro-sized specimens can yet provide information on local properties under tension within the ORL for specimens with constant oxygen content compared to oxygen-graded samples such as pre-oxidized specimens. The loss in mechanical properties of the pre-oxidized specimen can be structural based on the gradient of properties and stress distribution within the specimen gage section. Smaller scale tensile testing might be of interest to better document the local tensile properties within the ORL as a function of the oxygen concentration.

As far as the ORL/gage section ratio is concerned, elastic simulations of the oxygen-graded materials, *i.e.*, the pre-oxidized specimens, demonstrated that short oxidation exposures and thick specimens lead to higher stress levels both at the metal/oxide interface and in the specimen core. In other words, such conditions might favor ORL cracking at slightly lower macroscopic stress levels but also can lead to onset of microplasticity or viscoplastic behavior in the specimen core and strain localization at the

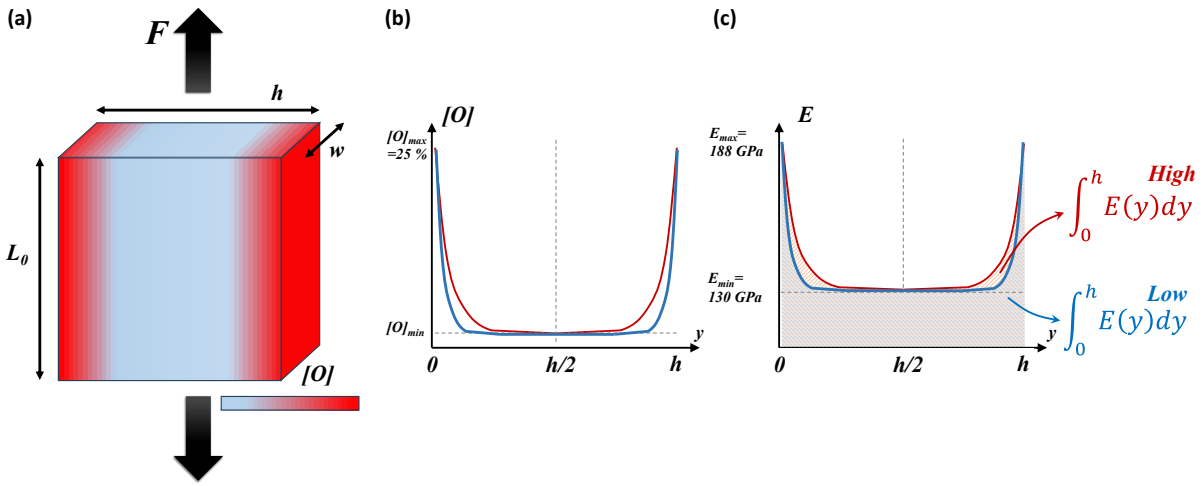

Figure 14: (a) Schematic illustration of the oxygen-graded material and load application, (b) Illustration of two different oxygen distribution profiles (blue = short oxidation time and red = long oxidation time), (c) Illustration of the distribution of elastic properties for both cases. The colored region below curves corresponds to the integral term of the elastic profile.

microstructure scale. It is worth noting that longer oxidation exposures have a beneficial effect on the stress level encountered both at the specimen surface and specimen core. Despite lower values of stress for thinner specimens at a similar depth from the metal/oxide interface, *i.e.*, at given oxygen concentration, thin specimens failed at lower macroscopic stress levels due to extension of the ORL and reduction of the effective load-bearing section after ORL cracking. Furthermore, based on homothetic considerations for oxidation time/specimen thickness of specimens with a similar ORL/gage section ratio, stress distribution profiles are elastically identical, confirming the linearity of yield strength/fracture strength as a function of the ORL/gage section ratio (Fig. 7(c)). Steady-stress during oxidation was recently found to lower the oxygen concentration at the metal/oxide and slightly increase the apparent diffusion of O within Ti, leading to deeper ORL under stress compared to simple oxidation [31]. Therefore, the effect of external stresses on service components have to be taken into account to evaluate stress distribution during service and the potential of ORL cracking.

In addition to the numerical simulations of stress distribution in the oxygen-graded titanium, analytical approximations can be proposed using homogenization scheme of the graded material. In the particular case of oxidation diffusion front being parallel to the further loading direction, as depicted in Fig. 14(a), a Voigt homogenization model could inform on local stress distribution in the mechanically-graded material, in which each layer experiences an identical deformation.

The load F, applied onto the oxygen-graded material with a thickness h and a width w, is linked to the homogeneous stress σ_{hom} as follows:

$$F = \sigma_{hom}.h.w \tag{5}$$

Similarly, F is related to the local stress profile using the following relationship:

$$F = w.\int_0^h \sigma(y)\,dy \tag{6}$$

Considering the local variation of elastic properties (Fig. 14(c)) due to oxygen ingress into titanium (Fig. 14(b)), F can be related to the local elastic properties $E(x)$ along the thickness direction y since the deformation ϵ of each material layer is considered identical (Voigt model, *i.e.*, isodeformation model).

$$F = w.\epsilon.\int_0^h E(y)\,dy \tag{7}$$

Since the local deformation is identical for each material layer, the global deformation aims to link the local and homogeneous stress using the following expression:

$$\epsilon = \frac{h.\sigma_{hom}}{\int_0^h E(y)\,dy} \tag{8}$$

Therefore, the local stress can be related to the distribution of elastic properties along the width, as follows:

$$\frac{\sigma_{max}}{\sigma_{hom}} = \frac{h.E_{max}}{\int_0^h E(y)\,dy} \tag{9}$$

$\int_0^h E(y)\,dy$ is directly related to the oxidation duration and increases with oxidation duration, as shown in Fig. 14(c). For a given h and σ_{hom}, σ_{max} increase when $\int_0^h E(y)\,dy$ decreases. Therefore, this approach justifies maximal stresses observed at the surface and in the specimen core for shorter oxidation durations (greater $\int_0^h E(y)\,dy$) for a given specimen thickness h. Similarly, this formulation depicts maximal stresses at the surface and core for thicker specimens (greater h) for a given oxidation duration ($\int_0^h E(y)\,dy$). This analytical approach aims at demonstrating the "core/shell" effects demonstrated using finite element simulations (Fig. 11 and 12).

Depending on their processing route, titanium and titanium alloys can present fine grain structures with relatively low crystallographic texture or relatively coarse grains with pronounced crystallographic textures, as investigated in the present study. Former β-grain heritage, microtextured regions or feather-like structures can lead to heterogeneous strain distribution at the microstructure scale, leading to micro and mesoscopic stress/strain concentration, as observed for the virgin Ti64 in Fig. 5(b) and reported in the literature [58, 59, 60, 61, 62]. While ORL cracking might be sensitive to crystallographic orientation in regard to the macroscopic loading, ORL cracking in large grain/colony structures can also be influence by the onset of plasticity with grain/colony beneath the ORL, leading to intense slip/strain localization. This case is particularly encountered for thin ORL/large grains, where inclined strain localization inherent to microplasticity of the sub-ORL material is sufficient to locally crack the ORL, as observed in Fig. 5(c). Therefore, the ORL thickness/grain size ratio might be of interest for further consideration on the variability and distribution of ORL cracking on the specimen gage.

4.3. Size effects on the oxygen distribution

In the present study, oxygen distribution in the ORL was of importance in order to evaluate the extension of the ORL and its influence on the mechanical integrity of thin specimens. It is important to note that oxygen distribution was solely characterized using EPMA on thick specimens, meeting the semi-infinite condition in terms of unidirectional solid-state diffusion scheme. This consideration is necessary to accurately identify the coefficient of diffusion using analytical diffusion equations [54, 55]. In addition, the specimen preparation and pre-oxidation was also of importance in order to assure a reproducible oxygen concentration at the metal oxide/interface, then oxide surface after oxide removal. This concentration is critical in the evaluation of the coefficient of diffusion and is highly dependent on the specimen preparation but also the oxidation atmospheres (presence of water in air, *i.e.*, dry air, wet air versus laboratory air, temperature, thermal loading, etc.) [57]. The specimen preparation with the precision Jig and standardized metallographic preparation aimed to repeatable surface finish [51]. In addition, pre-oxidations in the same batch also favored such a reproducibility. The particular care in specimen preparation was confirmed by the reproducibility in measured oxygen concentration at the metal/oxide interface using EPMA analyses. For thin specimens, the semi-infinite medium condition is not met anymore and the previous analytical solution is invalid. Therefore, finite-element or discrete-element simulations have to be considered in order to evaluate the distribution of oxygen [29]. Oxygen profiles were simulated for thin specimens for which semi-infinite conditions are not met. For these simulations, both the oxygen flux and oxygen concentration at the metal/oxide interface were considered to not be influenced by the specimen thickness. In other word, similar oxidation and diffusion boundary conditions were considered, regardless of the specimen thickness and oxygen increase in the specimen core. Such hypotheses have to be experimentally verified, but were not possible in the present investigation. Our motivation was to evaluate the pre-oxidation time/specimen thickness conditions leading to an enrichment in oxygen of the specimen core. In addition, both oxygen concentration at the metal /oxide interface and oxygen coefficient of diffusion were considered constant during the whole simulation. Simulations highlight that deviation of oxygen distribution in titanium from the conventional "erf" function occurs due to the significant oxygen enrichment of the core of the sample. The influence of the local oxygen content on the local oxygen coefficient of diffusion as well as the influence of the local stress on oxygen diffusion are not taken into account in the present study. Such considerations could be implemented along with experimental measurement of oxygen concentration profiles for thin specimens and will be part of future works.

5. Conclusions

The influence of oxygen insertion in a titanium alloy due to high temperature oxidation was investigated on the tensile behavior of pre-oxidized Ti64 alloy. Tensile tests of ultrathin specimens with different extensions of an oxygen-rich layer (ORL) were conducted, alongside nanoindentation and EPMA profiles to correlate local mechanical properties to the oxygen concentration. The different micromechanical approaches aimed to highlight:

- a competition between oxygen strengthening in the ORL due to oxygen insertion under compression and embrittlement under tension leading to a drop of mechanical strength of the pre-oxidized specimens ;
- a decrease of the mechanical strength and ductility of pre-oxidized specimen for longer oxidation time of thinner specimens ;
- a linear increase of stiffness with the increase in oxygen concentration using nanoindentation ;
- a contribution of strain localization at the microstructure scale beneath the ORL on the ORL cracking using digital image correlation techniques ;
- stress distribution profiles are dependent on the ORL/specimen thickness ratio due to core/shell effects using finite element method to simulate both oxygen profiles in thin specimens and stress distribution during an elastic loading.

6. License

7. Acknowledgements

This work was supported by the European Research Council [project HT-S_4DefOx - Grant number 948007]. This work was also partly supported by the Agence Nationale de la Recherche (ANR) [ANR-18-CE08-0003]. The authors particularly acknowledge Sophie GOUY from the Raimond Castaing Microanalysis Centre (UAR 3623) for performing EPMA analyses. The authors are grateful to R. Mainguy (CIRIMAT) for specimen machining and J.-C. Passieux (ICA) for new developments in https://github.com/jcpassieux/pyxel. The authors would also like to extend their thanks to Karine Vieillevigne (ICA) for help with specimen preparation and SEM observations.

8. Data Availability

The raw/processed data required to reproduce these findings cannot be shared at this time as the data also forms part of an ongoing study.

9. Declaration of competing interests

The authors declare that they have no known competing financial interests or personal relationships that could have appeared to influence the work reported in this paper.

References

1. Boyer, R.. An overview on the use of titanium in the aerospace industry. *Materials Science and Engineering: A* 1996;213(1):103–114. doi:https://doi.org/10.1016/0921-5093(96)10233-1; international Symposium on Metallurgy and Technology of Titanium Alloys.
2. Peters, M., Kumpfert, J., Ward, C.H., Leyens, C.. Titanium alloys for aerospace applications. *Advanced Engineering Materials* 2003;5(6):419–427. doi:10.1002/adem.200310095.
3. Murray, J.L., Wriedt, H.A.. The O-Ti (Oxygen-Titanium) system. *Journal of Phase Equilibria* 1987;8(2):148–165. doi:10.1007/BF02873201.
4. Kofstad, P., Anderson, P.B., Krudtaa, O.J.. Oxidation of titanium in the temperature range 800-1200°C. *Journal of The Less-Common Metals* 1961;3(2):89–97. doi:10.1016/0022-5088(61)90001-7.
5. Dupressoire, C., Rouaix-Vande Put, A., Emile, P., Archambeau-Mirguet, C., Peraldi, R., Monceau, D.. Effect of nitrogen on the kinetics of oxide scale growth and of oxygen dissolution in the Ti6242S titanium-based alloy. *Oxidation of Metals* 2017;87(3):343–353. doi:10.1007/s11085-017-9729-1.
6. Vaché, N., Monceau, D.. Oxygen Diffusion Modeling in Titanium Alloys: New Elements on the Analysis of Microhardness Profiles. *Oxidation of Metals* 2020;93(1-2):215–227. doi:10.1007/s11085-020-09956-9.
7. Casadebaigt, A., Hugues, J., Monceau, D.. High temperature oxidation and embrittlement at 500–600 C of Ti-6Al-4V alloy fabricated by Laser and Electron Beam Melting. *Corrosion Science* 2020;175:108875. doi:10.1016/j.corsci.2020.108875.
8. Casadebaigt, A., Monceau, D., Hugues, J.. Oxygen embrittlement kinetics at 500 – 600 C of the Ti-6Al-4V alloy fabricated by Laser and Electron Powder Bed Fusion. *high temperature corrosion and protection of materials* 2024;XXX:XXX. doi:underreview.
9. Finlay, W.L., Snyder, J.A.. Effects of three interstitial solutes (nitrogen, oxygen, and carbon) on the mechanical properties of high-purity, alpha titanium. *JOM* 1950;2(2):277–286. doi:10.1007/BF03399001.
10. Beevers, C., Robinson, J.. Some observations on the influence of oxygen content on the fatigue behaviour of α-titanium. *Journal of The Less-Common Metals* 1969;17(4):345–352. doi:10.1016/0022-5088(69)90061-7.
11. Shamblen, C.E., Redden, T.. Air contamination and embrittlement of titanium alloys. In: *The Science, Technology and Application of Titanium*. London (UK); 1970:199–208. doi:10.1016/B978-0-08-006564-9.50027-0.
12. Baur, G., Lehr, P.. Influence spécifique de l'oxygène sur quelques propriétés physiques, les caractéristiques mécaniques et la dynamique de déformation plastique du titane de haute pureté. *Journal of The Less-Common Metals* 1980;69(1):203–218. doi:10.1016/0022-5088(80)90055-7.
13. Conrad, H.. Effect of interstitial solutes on the strength and ductility of titanium. *Progress in Materials Science* 1981;26(2):123–403. doi:https://doi.org/10.1016/0079-6425(81)90001-3.
14. Bendersky, L., Rosen, A.. The effect of exposure on the mechanical properties of the Ti-6Al-4v alloy. *Engineering Fracture Mechanics* 1984;20(2):303–311. doi:10.1016/0013-7944(84)90135-8.
15. Shenoy, R., Unnam, J., Clark, R.. Oxidation and embrittlement of Ti-6Al-2Sn-4Zr-2Mo alloy. *Oxidation of Metals* 1986;26(1-2):105–124. doi:10.1007/BF00664276.
16. Wasz, M., Brotzen, F., McLellan, R., Griffin, A.. Effect of oxygen and hydrogen on mechanical properties of commercial purity titanium. *International Materials Reviews* 1996;41(1):1–12. doi:10.1179/imr.1996.41.1.1.
17. Parthasarathy, T.A., Porter, W.J., Boone, S., John, R., Martin, P.. Life prediction under tension of titanium alloys that develop an oxygenated brittle case during use. *Scripta Materialia* 2011;65(5):420–423. doi:https://doi.org/10.1016/j.scriptamat.2011.05.025.
18. Brandes, M.C., Baughman, M., Mills, M.J., Williams, J.C.. The effect of oxygen and stress state on the yield behavior of commercially pure titanium. *Materials Science and Engineering A* 2012;551:13–18. doi:10.1016/j.msea.2012.04.058.
19. Yan, M., Xu, W., Dargusch, M.S., Tang, H.P., Brandt, M., Qian, M.. Review of effect of oxygen on room temperature ductility of titanium and titanium alloys. *Powder Metallurgy* 2014;57(4):251–257. URL: https://doi.org/10.1179/1743290114Y.0000000108. doi:10.1179/1743290114Y.0000000108.
20. Hornberger, H., Randow, C., Fleck, C.. Fatigue and surface structure of titanium after oxygen diffusion hardening. *Materials Science and Engineering A* 2015;630:51–57. doi:10.1016/j.msea.2015.02.006.
21. Hidalgo, A.A., Ebel, T., Limberg, W., Pyczak, F.. Influence of oxygen on the fatigue behaviour of Ti-6Al-7Nb alloy. *Key Engineering Materials* 2016;704:44–52. doi:10.4028/www.scientific.net/KEM.704.44.
22. Satko, D., Shaffer, J., Tiley, J., Semiatin, S., Pilchak, A., Kalidindi, S., Kosaka, Y., Glavicic, M., Salem, A.. Effect of microstructure on oxygen rich layer evolution and its impact on fatigue life during high-temperature application of α/β titanium. *Acta Materialia* 2016;107:377–389. doi:10.1016/j.actamat.2016.01.058.
23. Ren, J.Q., Wang, Q., Lu, X.F., Liu, W.F., Zhang, P.L., Zhang, X.B.. Effect of oxygen content on active deformation systems in pure titanium polycrystals. *Materials Science and Engineering A* 2018;731(April):530–538. doi:10.1016/j.msea.2018.06.083.
24. Texier, D., Sirvin, Q., Velay, V., Salem, M., Monceau, D., Mazères, B., Andrieu, E., Roumiguier, R., Dod, B.. Oxygen / nitrogen-assisted embrittlement of titanium alloys exposed at elevated temperature. *MATEC Web Conf* 2020;321:06004. doi:10.1051/matecconf/202032106004.
25. Sirvin, Q., Texier, D., Genée, J., Velay, V., Monceau, D., Dod, B.. Oxygen content effect on mechanical behavior of CP titanium exposed at elevated temperature. In: *Titanium 2023*. Edimbourg; 2023:.
26. Amherd Hidalgo, A., Ebel, T., Frykholm, R., Carreño-Morelli, E., Pyczak, F.. High-oxygen MIM Ti-6Al-7Nb: Microstructure, tensile and fatigue properties. *Materials Today Communications* 2023;34(August 2022). doi:10.1016/j.mtcomm.2022.104982.
27. Rosa, C.J.. Oxygen diffusion in alpha and beta titanium in the temperature range of 932 to 1142C. *Metallurgical Transactions* 1970;1:2517–2522. doi:10.1007/978-3-319-45713-0_10.
28. Gaddam, R., Sefer, B., Pederson, R., Antti, M.L.. Oxidation and alpha-case formation in Ti-6Al-2Sn-4Zr-2Mo alloy. *Materials Characterization* 2015;99:166–174. doi:10.1016/j.matchar.2014.11.023.
29. Ciszak, C., Monceau, D., Desgranges, C.. Modelling the high temperature oxidation of titanium alloys: Development of a new numerical tool PyTiOx. *Corrosion Science* 2020;176. doi:10.1016/j.corsci.2020.109005.

30. Abdallah, I., Dupressoire, C., Laffont, L., Monceau, D., Vande Put, A.. STEM-EELS identification of TiO X N Y , TiN, Ti 2 N and O, N dissolution in the Ti2642S alloy oxidized in synthetic air at 650 C. *Corrosion Science* 2019;153:191–199. doi:10.1016/j.corsci.2019.03.037.
31. Cavé, K., Texier, D., Vallot, S., Chanfreau, N., Fessler, E., Dehmas, M., Monceau, D., Poquillon, D.. Effect of creep loading on the oxygen diffusion of Ti6242S at 650 C. *Scripta Materialia* 2023;:submitted.
32. Dupressoire, C., Descoins, M., VandePut, A., Epifano, E., Mangelinck, D., Emile, P., Monceau, D.. The role of nitrogen in the oxidation behaviour of a Ti6242S alloy: a nanoscale investigation by atom probe tomography. *Acta Materialia* 2021;216:117134. doi:10.1016/j.actamat.2021.117134.
33. Relationship between the volume of the unit cell of hexagonal-close-packed Ti, hardness and oxygen content after α-case formation in Ti-6Al-2Sn-4Zr-2Mo-0.1Si alloy. *Journal of Applied Crystallography* 2016;49(1988):175–181. doi:10.1107/S1600576715022906.
34. Ciszak, C., Popa, I., Brossard, J.M., Monceau, D., Chevalier, S.. NaCl induced corrosion of Ti-6Al-4V alloy at high temperature. *Corrosion Science* 2016;110:91–104. doi:10.1016/j.corsci.2016.04.016.
35. Radecka, A., Coakley, J., Vorontsov, V., Martin, T., Bagot, P., Moody, M., Rugg, D., Dye, D.. Precipitation of the ordered $\alpha 2$ phase in a near-α titanium alloy. *Scripta Materialia* 2016;117:81–85. doi:10.1016/j.scriptamat.2016.02.015.
36. Poquillon, D., Armand, C., Huez, J.. Oxidation and oxygen diffusion in Ti-6al-4V alloy: Improving measurements during SIMS analysis by rotating the sample. *Oxidation of Metals* 2013;79(3-4):249–259. doi:10.1007/s11085-013-9360-8.
37. Oh, J., Lee, B., Cho, S.W., Lee, S.W., Choi, G.S., Lim, J.W.. Oxygen effects on the mechanical properties and lattice strain of Ti and Ti-6Al-4V. *Metals and Materials International* 2011;17(5):733–736. doi:10.1007/s12540-011-1006-2.
38. Vicente, F.B., Correa, D.R.N., Donato, T.A.G., Arana-Chavez, V.E., Buzalaf, M.A.R., Grandini, C.R.. The influence of small quantities of oxygen in the structure, microstructure, hardness, elasticity modulus and cytocompatibility of Ti-Zr alloys for dental applications. *Materials* 2014;7(1):542–553. doi:10.3390/ma7010542.
39. Magazzeni, C.M., Gardner, H.M., Howe, I., Gopon, P., Waite, J.C., Rugg, D., Armstrong, D.E., Wilkinson, A.J.. Nanoindentation in multi-modal map combinations: a correlative approach to local mechanical property assessment. *Journal of Materials Research* 2021;36(11):2235–2250. doi:10.1557/s43578-020-00035-y.
40. Cai, Z., Xiang, T., Bao, W., Chen, J., Gao, T., Xie, G.. Enhancing strength and ductility of pure titanium by interstitial oxygen atoms. *Materials Science, SSRN Electronic Journal* 2022;14(2).
41. Texier, D., Sirvin, Q., Dziri, A., Proudhon, H., Yastrebov, V., Legros, M.. Effect of oxygen content on the sub-grain nanoindentation response in titanium affected by high temperature oxidation. In: *Titanium 2023*. Edimbourg; 2023:.
42. Kværndrup, F., Kücükyildiz, Ö., Winther, G., Somers, M., Christiansen, T.. Extreme hardening of titanium with colossal interstitial contents of nitrogen and oxygen. *Materials Science and Engineering A* 2021;813:141033. doi:10.1016/j.msea.2021.141033.
43. Lee, Y., Welsch, G.. Young's modulus and damping of Ti6Al4V alloy as a function of heat treatment and oxygen concentration. *Materials Science and Engineering A* 1990;128(1):77–89. doi:10.1016/0921-5093(90)90097-M.
44. Kwasniak, P., Muzyk, M., Garbacz, H., Kurzydlowski, K.. Influence of oxygen content on the mechanical properties of hexagonal Ti-First principles calculations. *Materials Science and Engineering A* 2014;590:74–79. doi:10.1016/j.msea.2013.10.004.
45. Baillieux, J., Archambeau, C., Emile, P., Poquillon, D.. Effet de la diffusion de l'oxygène sur le comportement mécanique du Ti–6Al–2Sn–4Zr– 2Mo–0.1Si. In: *CFM2015*. Lyon (France); 2015:22–25.
46. Britton, T., Liang, H., Dunne, F., Wilkinson, A.. The effect of crystal orientation on the indentation response of commercially pure titanium: experiments and simulations. In: *Proc. R. Soc. A*. Jakson Lake (USA); 2010:466695—-719. doi:http://doi.org/10.1098/rspa.2009.0455.
47. Fizanne-Michel, C., Cornen, M., Castany, P., Péron, I., Gloriant, T.. Determination of hardness and elastic modulus inverse pole figures of a polycrystalline commercially pure titanium by coupling nanoindentation and ebsd techniques. *Materials Science and Engineering: A* 2014;613:159–162. doi:https://doi.org/10.1016/j.msea.2014.06.098.
48. Weaver, J., Priddy, M., McDowell, D., Kalidindi, S.. On capturing the grain-scale elastic and plastic anisotropy of alpha-Ti with spherical nanoindentation and electron back-scattered diffraction. *Acta Materialia* 2016;117:23–34. doi:10.1016/j.actamat.2016.06.053.
49. Jabir, H., Fillon, A., Castany, P., Gloriant, T.. Crystallographic orientation dependence of mechanical properties in the superelastic ti-24nb-4zr-8sn alloy. *Phys Rev Mater* 2019;3:063608–18. doi:10.1103/PhysRevMaterials.3.063608.
50. Barkia, B., Doquet, V., Couzinié, J.P., Guillot, I., Héripré, E.. In situ monitoring of the deformation mechanisms in titanium with different oxygen contents. *Materials Science and Engineering A* 2015;636:91–102. doi:10.1016/j.msea.2015.03.044.
51. Texier, D., Monceau, D., Salabura, J.C., Mainguy, R., Andrieu, E.. Micromechanical testing of ultrathin layered material specimens at elevated temperature. *Materials at high temperatures* 2016;33(4-5):325–337. doi:10.1080/09603409.2016.1182250.
52. Passieux, J.c., Bouclier, R., Périé, J.n.. A space-time PGD-DIC algorithm. *Experimental Mechanics* 2018;58(7):1195–1206. doi:10.1007/s11340-018-0387-2.
53. Oliver, W., Pharr, G.. Measurement of hardness and elastic modulus by instrumented indentation: Advances in understanding and refinements to methodology. *Journal of Materials Research* 2004;19(1):3–20. doi:https://doi.org/10.1557/jmr.2004.19.1.3.
54. Fick, A.. Ueber Diffusion. *Annalen der Physik* 1855;170(1):59–86. doi:https://doi.org/10.1002/andp.18551700105.
55. Crank, J.. The mathematics of diffusion. 1956:.
56. Combescure, A., Hoffmann, A., Pasquet, P.. The CASTEM Finite Element System. Berlin, Heidelberg: Springer Berlin Heidelberg; 1982:115–125. doi:10.1007/978-3-662-07229-5_8.
57. Vaché, N., Cadoret, Y., Dod, B., Monceau, D.. Modeling the oxidation kinetics of titanium alloys: Review, method and application to Ti-64 and Ti-6242s alloys. *Corrosion Science* 2021;178:109041. doi:10.1016/j.corsci.2020.109041.
58. Echlin, M.P., Stinville, J.C., Miller, V.M., Lenthe, W.C., Pollock, T.M.. Incipient slip and long range plastic strain

localization in microtextured Ti-6Al-4V titanium. *Acta Materialia* 2016;114:164–175. doi:10.1016/j.actamat.2016.04.057.

59. Lunt, D., da Fonseca, J.Q., Rugg, D., Preuss, M.. Microscopic strain localisation in Ti-6Al-4V during uniaxial tensile loading. *Materials Science and Engineering A* 2017;680:444–453. doi:10.1016/j.msea.2016.10.099.
60. Hémery, S., Dang, V.T., Signor, L., Villechaise, P.. Influence of Microtexture on Early Plastic Slip Activity in Ti-6Al-4V Polycrystals. *Metallurgical and Materials Transactions A: Physical Metallurgy and Materials Science* 2018;49(6):2048–2056. doi:10.1007/s11661-018-4569-4.
61. Yvinec, T., Naït-Ali, A., Mellier, D., Bertheau, D., Cormier, J., Villechaise, P., Rat, L., Hémery, S.. Tensile properties of Ti-6Al-4V as-built by laser metal deposition: The relationship between heat affected zone bands, strain localization and anisotropy in ductility. *Additive Manufacturing* 2022;55. doi:10.1016/j.addma.2022.102830.
62. Rouwane, A., Texier, D., Hémery, S., Passieux, J.C., Sirvin, Q., Genée, J., Proietti, A., Stinville, J.C.. Strain localization in Ti and Ti-allys using three-dimensional topographic imaging. In: *Titanium 2023*. 2023:.